



Possible Progression of Mass-flow Processes around Young Intermediate-mass Stars Based on High-resolution Near-infrared Spectroscopy. I. Taurus

Chikako Yasui^{1,2}, Satoshi Hamano^{1,2} , Kei Fukue², Sohei Kondo^{3,2}, Hiroaki Sameshima⁴ , Keiichi Takenaka^{2,5}, Noriyuki Matsunaga^{6,2}, Yuji Ikeda^{2,7} , Hideyo Kawakita^{2,5} , Shogo Otsubo², Ayaka Watase^{2,5}, Daisuke Taniguchi⁶ , Misaki Mizumoto⁸ , Natsuko Izumi^{9,1,2} , and Naoto Kobayashi^{4,3,2}

¹ National Astronomical Observatory of Japan, 2-21-1 Osawa, Mitaka, Tokyo 181-8588, Japan; ck.yasui@nao.ac.jp

² Laboratory of Infrared High-resolution spectroscopy (LIH), Koyama Astronomical Observatory, Kyoto Sangyo University, Mo-toyama, Kamigamo, Kita-ku, Kyoto 603-8555, Japan

³ Kiso Observatory, Institute of Astronomy, School of Science, The University of Tokyo, 10762-30, Mitake, Kiso-machi, Kiso-gun, Nagano 397-0101, Japan

⁴ Institute of Astronomy, The University of Tokyo, 2-21-1 Osawa, Mitaka, Tokyo 181-0015, Japan

⁵ Department of Astrophysics and Atmospheric Sciences, Faculty of Sciences, Kyoto Sangyo University, Motoyama, Kamigamo, Kita-ku, Kyoto 603-8555, Japan

⁶ Department of Astronomy, Graduate School of Science, The University of Tokyo, 7-3-1 Hongo, Bunkyo-ku, Tokyo 113-0033, Japan

⁷ Photocoding, 460-102 Iwakura-Nakamachi, Sakyo-ku, Kyoto, 606-0025, Japan

⁸ Centre for Extragalactic Astronomy, Department of Physics, University of Durham, South Road, Durham DH1 3LE, UK

⁹ College of Science, Ibaraki University, 2-1-1 Bunkyo, Mito, Ibaraki 310-8512, Japan

Received 2018 December 25; revised 2019 September 11; accepted 2019 September 17; published 2019 November 27

Abstract

We used the WINERED spectrograph to perform near-infrared high-resolution spectroscopy (resolving power $R = 28,000$) of 13 young intermediate-mass stars in the Taurus star-forming region. Based on the presence of near- and mid-infrared continuum emission, young intermediate-mass stars can be classified into three different evolutionary stages: Phases I, II, and III in the order of evolution. Our obtained spectra ($\lambda = 0.91\text{--}1.35\ \mu\text{m}$) depict He I $\lambda 10830$ and $P\beta$ lines that are sensitive to magnetospheric accretion and winds. We also investigate five sources each for $P\beta$ and He I lines that were obtained from previous studies along with our targets. We observe that the $P\beta$ profile morphologies in Phases I and II corresponded to an extensive variety of emission features; however, these features are not detected in Phase III. We also observe that the He I profile morphologies are mostly broad subcontinuum absorption lines in Phase I, narrow subcontinuum absorption lines in Phase II, and centered subcontinuum absorption features in Phase III. Our results indicate that the profile morphologies exhibit a progression of the dominant mass-flow processes: stellar wind and probably magnetospheric accretion in the very early stage, magnetospheric accretion and disk wind in the subsequent stage, and no activities in the final stage. These interpretations further suggest that opacity in protoplanetary disks plays an important role in mass-flow processes. Results also indicate that He I absorption features in Phase III sources, associated with chromospheric activities even in such young phases, are characteristics of intermediate-mass stars.

Key words: accretion, accretion disks – infrared: stars – protoplanetary disks – stars: formation – stars: pre-main sequence – stars: winds, outflows

1. Introduction

Stars are formed owing to the gravitationally induced collapse of cold molecular gas. While the molecular clouds are contracted during the collapse, the initial rotation of the star-forming cloud is enormously magnified by the conservation of angular momentum. In this process, the rotating circumstellar disks are formed, and the majority of the material of a typical star is accreted through its disk (Hartmann 2009). Although almost all of the angular momentum (>99%) must be removed to form an observable star, we lack a conclusive theory explaining the mechanics of the angular momentum transfer (“angular momentum problem”; Bodenheimer 1995). As one of the most important processes, this study focuses on the mass-flow processes occurring very close (radius $r \lesssim 1$ au) to central stars. In this region, a large population of close-in planetary systems has been reported, even around young stellar objects (YSOs) younger than 10 Myr (e.g., Donati et al. 2016). However, the manner in which planets are formed is still being debated (Winn & Fabrycky 2015). Because the interaction between the stars and disks at which planets are formed occurs mainly in the inner disk region, it is essential to investigate the conditions of this region from the planet formation viewpoint.

As for mass-flow processes, magnetospheric accretion and outflowing gas have been proposed. Because direct imaging for separations of less than 1 au is considered to be very difficult using existing instruments, spectroscopy has been employed. Traditionally, H α , NaD, Ca II H&K, and Mg II h&k lines have been used to conduct diagnostics (e.g., Mundt 1984; Calvet & Hartmann 1992). For mass accretion, these diagnostics have permitted the development of a general picture with respect to various factors, including the mass accretion rate, evolution, geometry, and stellar mass dependence (e.g., Hartmann et al. 1998; Muzerolle et al. 1998b, 2004; Calvet et al. 2004). However, the actual mechanics of outflowing gas have not yet been completely elucidated. There are at least three possible configurations of wind formation: a disk wind (Ustyugova et al. 1995), an X-wind (Shu et al. 1994), and a stellar wind (Hartmann et al. 1982). To distinguish between different theoretical models, constraints on the nature or location of the wind-launching region are very important. However, the aforementioned traditional spectral lines exhibit blueshifted absorption superposed on the broad emission features. This observation signifies the presence of high-velocity wind close to the star (Ardila et al. 2002), yielding little information on the nature or location of the wind-launching region.

Recently, the He I 10830 Å line has been suggested as a particularly suitable and sensitive probe of both mass accretion and outflow (Edwards et al. 2006). Edwards et al. (2006) reported that $\sim 70\%$ of their sample of 39 classical T Tauri stars (CTTSs) exhibit a blueshifted subcontinuum absorption that can be assumed to be a probe of outflow. This is in contrast to H α , for which only $\sim 10\%$ of the stars show a similar type of absorption component. Additionally, $\sim 50\%$ of their CTTSs show redshifted absorption below the continuum in He I; this can be considered a probe of mass accretion. The authors also highlighted that the direct probes of the launch region of the outflowing gas can only be created by high-resolution spectroscopy of the He I line. While the targets for Edwards et al. (2006) were primarily low-mass stars, Oudmaijer et al. (2011) and Cauley & Johns-Krull (2014) presented a He I $\lambda 10830$ profile for Herbig Ae/Be stars (HAeBes), which are intermediate-mass pre-main-sequence stars. The calculated He I model profile (e.g., Kwan et al. 2007; Fischer et al. 2008; Kurosawa et al. 2011; Kurosawa & Romanova 2012) suggests that the mass-flow processes occurring in the inner part of the protoplanetary disks (disk wind, stellar wind, and magnetospheric accretion) can be distinguished based on the He I profile morphologies. Furthermore, the hydrogen Paschen series can also serve as diagnostics for magnetospheric accretion. Because the opacity of these series lines is lower than that of the H α lines, they more clearly depict signatures of infall of accreting material in a magnetospheric funnel flow, whereas H α often does not show such signatures (Muzerolle et al. 2001). Folha & Emerson (1999, 2001) presented the P β line profiles for 49 T Tauri stars and observed that inverse P Cygni profile features, indicating magnetospheric mass accretion, can be observed at a relatively high frequency even though blueshifted absorption features are absent. Edwards et al. (2006) also presented the P γ line profiles for 48 T Tauri stars. The calculated model profiles of the Paschen lines (e.g., Kurosawa et al. 2011; Kurosawa & Romanova 2012) suggest that the existence or absence of magnetospheric accretion can be determined based on the line morphology; however, these lines cannot serve as diagnostics for winds.

The progression of the dominant mass-flow processes through stellar evolution should also impose constraints on the mechanistic theories. Edwards et al. (2006) proposed a progression involving veilings, which are considered to be correlated with the mass accretion rate (e.g., Beristain et al. 2001). In particular, these authors suggested that the emission equivalent width (EW) of P γ decreases with decreasing veiling. Based on He I profiles, Kwan et al. (2007) used a comparison of their theoretical line profiles with the profiles observed by Edwards et al. (2006) to suggest that the wind signatures of stars with high disk accretion rates are more likely to indicate stellar wind than disk wind. Furthermore, although a moderate trend is evident in these factors, this pattern does not seem to be valid for all the stellar sources. This inconsistency may be attributed to an extensive variety of disk properties that have been revealed by recent observational studies, e.g., mass accretion rate, disk lifetime, and disk mass. The median disk lifetime has been estimated to be approximately 3 Myr even though the lifetimes vary from less than 1 Myr to a maximum of 10 Myr. The mass accretion rate and disk mass also exhibit large dispersions, $\sim \pm 1$ dex (for the mass accretion rate, see Figures 2 and 3 in Hartmann 2008; for the disk mass, see Figure 5 in Williams & Cieza 2011 and Figure 7 in Ansdell et al. 2017); further, because the entirety of dust and gas in the inner

and outer disks is dispersed almost simultaneously; at $\lesssim 0.5$ Myr (Williams & Cieza 2011), there appear to be no clear indicators of the protoplanetary disk evolutionary stages. However, this picture is obtained from low-mass stars ($\lesssim 1 M_{\odot}$), which constitute the majority in the solar neighborhood. Recent observations suggest that the protoplanetary disks surrounding the intermediate-mass stars show different evolutionary stages; for the intermediate-mass stars ($\gtrsim 1.5 M_{\odot}$), only the innermost disk regions that are traced with the near-infrared (NIR) *K*-band ($r \sim 0.3$ au) disperse at a very early time as compared to the outer disks by ~ 3 – 4 Myr (Yasui et al. 2014). Therefore, based on the presence of innermost and outer disks, the intermediate-mass stars can be categorized into three phases. Furthermore, the intermediate-mass stars should be appropriate targets for investigating the time variation of dominant mass-flow processes. Based on the He I line profiles, Cauley & Johns-Krull (2014) suggested that HAe stars exhibit signatures of magnetospheric accretion and stellar wind even though they do not exhibit disk wind. Although these authors have suggested that these processes are characteristic of intermediate-mass stars, this may only be valid for the Phase I sources to which the HAe stars are comparable. To bridge this gap, it is necessary to observe young intermediate-mass stars in all the evolutionary phases.

In this study, we present the results of a census of He I $\lambda 10830$ and P β in 13 young intermediate-mass stars in the Taurus star-forming region, which is one of the nearest active star-forming regions (distance of $D = 140$ pc; Kenyon et al. 2008). Given its proximity, this region can be investigated using X-ray to radio wavelengths, and the members of Taurus have been more comprehensively identified (from early-type stars to brown dwarfs) than those of any other star-forming region. Given the young age of the Taurus complex (~ 1.5 Myr; Barrado y Navascués & Martín 2003), most members are still surrounded by circumstellar materials. Therefore, Taurus is the best target for conducting our first star formation study with the Warm Infrared Echelle spectrograph for REalizing Decent infrared high-resolution spectroscopy (WINERED). WINERED is a spectrograph of high sensitivity and high resolution (with two resolution modes of $R = 28,000$ and $R = 70,000$), specifically customized for short NIR bands at 0.9 – $1.35 \mu\text{m}$ (Yasui et al. 2008). WINERED saw first light in 2012 May at the Araki 1.3 m telescope and is now attached to the New Technology Telescope (NTT; Ikeda et al. 2018). Moreover, it is planned to attach WINERED to the *Magellan* Telescope. We are continuing to investigate YSOs in the target star-forming regions, including Tr 37 and NGC 7160. By considering that the lifetime of the protoplanetary disks is approximately 10 Myr (e.g., Hernández et al. 2008), these regions are considered to be in different evolutionary phases than Taurus. Tr 37 (~ 4 Myr) is in the middle phase, while NGC 7160 (~ 10 Myr) is in the final phase. Our results for the other regions will be provided in a future work.

This study is organized as follows. In Section 2 we discuss the target selection, observations, and data reduction. In Section 3 we present the obtained spectra of the Paschen series and He I $\lambda 10830$ and determine the excess continuum emission and residual profiles. We further discuss the properties of the P β and He I $\lambda 10830$ lines. In Section 4 we discuss the statistics of the line profile morphologies and present an interpretation of the profile morphology of P β and He I $\lambda 10830$ in different evolutionary phases of the protoplanetary disks in combination with other intermediate-mass stars that have been

Table 1
Target List and Photometric Data

Object	R.A. (J2000.0)	Decl. (J2000.0)	SpT	J (mag)	H (mag)	K_S (mag)	α_{MIR}
(1)	(2)	(3)	(4)	(5)	(6)	(7)	(8)
V892 Tau	04:18:40.62	+28:19:15.5	B9	8.5	6.6	6.2	1.75
AB Aur	04:55:45.85	+30:33:04.3	A0	6.3*	5.5*	4.5*	-0.79
IRAS 04101+3103	04:13:20.02	+31:10:47.3	A1	9.2	8.7	8.1	0.97
HP Tau/G2	04:35:54.15	+22:54:13.6	G0	8.1	7.5	7.2	-0.43
RY Tau	04:21:57.41	+28:26:35.6	G1	7.2	6.1	5.4	-0.16
SU Aur	04:55:59.38	+30:34:01.5	G1	7.2	6.6	6.0	-0.32
HD 283572	04:21:58.84	+28:18:06.5	G5	7.4	7.0	6.9	-2.85
T Tau	04:21:59.43	+19:32:06.4	K0	7.2	6.2	5.3	-0.56
HBC 388	04:27:10.57	+17:50:42.6	K1	8.8	8.4	8.3	-2.78
RW Aur	05:07:49.57	+30:24:05.2	K3	8.4	7.6	7.0	-0.67
V773 Tau	04:14:12.92	+28:12:12.3	K3	7.5	6.6	6.2	-1.10
V410 Tau	04:18:31.11	+28:27:16.1	K3	8.4	7.8	7.6	-2.78
UX Tau	04:30:03.99	+18:13:49.4	K5	8.6	8.0	7.6	-1.99

Note. Column (4): spectral types from Furlan et al. (2006, 2011). Columns (5)–(7): NIR magnitude from the 2MASS PSC, J -band in Column (5), H -band in Column (6), and K_S -band magnitude in Column (7). Magnitudes for AB Aur are obtained from a study reported by Kenyon & Hartmann (1995), shown with the asterisks. Column (8): SED slope ($\alpha = d \ln \lambda F \lambda / d \ln \lambda$) with *Spitzer* IRS 6–13 μm presented in Furlan et al. (2006).

observed in previous studies. We further discuss the possible progression of dominant mass-flow processes in the evolution of protoplanetary disks. After comparing the results with those of the previous studies, we finally discuss the implications for theories of mass-flow processes.

2. Target Selection, Observation, and Data Reduction

2.1. Selection and Evolutionary Phase of Targets

We selected target intermediate-mass stars in the Taurus star-forming region. We defined stars within the mass range of $1.5\text{--}7 M_{\odot}$ as intermediate-mass stars (Yasui et al. 2014). The intermediate-mass stars were selected in a similar manner to that of Yasui et al. (2014); assuming a typical age of the Taurus star-forming region, ~ 1.5 Myr (Barrado y Navascués & Martín 2003), we obtained the spectral types of cluster members from the literature. For the lower mass limit, we used a spectral type of K5, corresponding to $1.5 M_{\odot}$. Although Yasui et al. (2014) set the upper limit mass at $7 M_{\odot}$ (spectral type B3), even the most massive stars in Taurus possess masses of $\sim 4 M_{\odot}$ (spectral type B9), which is substantially lower than the upper mass limit. Among the candidates selected above, the final targets are limited to stars with J -band magnitudes of less than 9 mag in the Two Micron All Sky Survey (2MASS) Point Source Catalog (PSC; Skrutskie et al. 2006). This criterion is required by the limited sensitivity of the Araki 1.3 m telescope’s implementation of WINERED, with which this study’s spectra can be obtained (see Section 2.2). Therefore, 13 target intermediate-mass stars were selected. The properties of the selected target stars are summarized in Table 1.

In a previous study (Yasui et al. 2014), we derived the intermediate-mass disk fraction in the NIR JHK photometric bands and in the mid-infrared (MIR) bands for young clusters in the age range of 0 to ~ 10 Myr. Yasui et al. (2014) have defined the region to the right of the border line¹⁰ (region highlighted in orange in Figure 1) as the disk excess region on $H - K$ versus

$J - H$ color-color diagram (Figure 1); stars located in the disk excess region are recognized as stars traced by NIR excess emissions. The MIR disk fraction is derived using *Spitzer* IRAC [3.6]–[8] photometric bands. The stars that have a spectral energy distribution (SED) slope with the MIR bands ($\alpha = d \ln \lambda F \lambda / d \ln \lambda$) of > -2.2 are recognized as stars traced by MIR excess emissions (Kennedy & Kenyon 2009). In the case of $2.5 M_{\odot}$ stars, NIR and MIR continuum emissions trace the innermost dust disk ($r \sim 0.3$ au) and the outer dust disk ($r \gtrsim 5$ au), respectively. Yasui et al. (2014) have suggested that in the very early phase, the intermediate-mass stars disperse only their innermost dust disks. They further disperse their outer dust disks with a time lag of $\sim 3\text{--}4$ Myr. Therefore, the presence of innermost disks and outer disks surrounding the intermediate-mass stars can be a clear evolutionary indicator. Hereafter, we refer to the three evolutionary phases of “Phase I”, which contains stars with both innermost and outer disks, “Phase II”, which contains stars without innermost disks but with outer disks, and “Phase III”, which contains stars without an innermost or outer disks.

The photometric data for 13 target intermediate-mass stars selected above are shown in Table 1. The data of NIR bands are obtained from the 2MASS PSC for targets, whose all JHK band photometric quality flags are denoted as “A” (signal-to-noise ratio, S/N, ≤ 10 for all JHK bands). Because AB Aur does not satisfy the condition, we used NIR data reported by Kenyon & Hartmann (1995). We plot our target sources in a $H - K$ versus $J - H$ diagram in Figure 1. Only four sources (V892 Tau, AB Aur, IRAS 04101+3103, and T Tau) are located in the disk excess region, suggesting that they have innermost dust disks. For MIR data, because IRAC photometric data for most target stars could not be obtained from the IRAC observations of the Taurus star-forming region (e.g., Hartmann et al. 2005), we adopted α values derived using *Spitzer* IRS within $\lambda = 6\text{--}13 \mu\text{m}$. Nine sources (V892 Tau, AB Aur, IRAS 04101+3103, RY Tau, SU Aur, T Tau, RW Aur, V773 Tau, and UX Tau) have α values of ≥ -2.2 , suggesting that they have outer dust disks. Therefore, the selected targets cover all the evolutionary phases of the protoplanetary disks, with four Phase I sources, five Phase II sources, and four Phase III sources. Four sources (V892 Tau, AB

¹⁰ The border line (the dot-dashed line) passes through the point of ($H - K_S$, $J - H$) = (0.2, 0) and is parallel to the reddening vector (shown with the gray arrow in Figure 1).

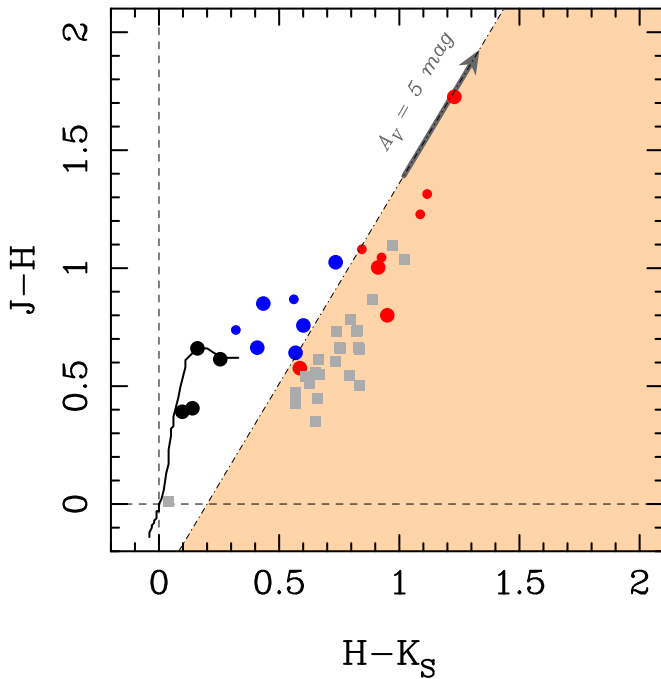


Figure 1. $H - K_S$ vs. $J - H$ color-color diagram. The dwarf track (Bessell & Brett 1988) is shown with a black line, while the reddening vector (Rieke & Lebofsky 1985) for $A_V = 5$ mag is shown with the gray arrow. The border line, which is parallel to the reddening vector and distinguishes H AeBe stars from other objects, is shown with a dot-dashed line. The region to the right of the border line (orange) is defined as the excess region for intermediate-mass stars (Yasui et al. 2014). Target intermediate-mass stars in this paper are shown with filled circles: Phase I, II, and III sources are shown with red, blue, and black, respectively. Six additional intermediate-mass stars in the samples of Folha & Emerson (2001) and Edwards et al. (2006) are denoted by small symbols with the same colors as the targets observed in the present study. H Ae stars in the sample of Cauley & Johns-Krull (2014) are shown with gray filled squares.

Aur, IRAS 04101+3103, and T Tau) are categorized into Phase I, five sources (RY Tau, SU Aur, T Tau, RW Aur, V773 Tau, and UX Tau) are categorized into Phase II, and four sources (HP Tau/G2, HD 283572, HBC 388, and V410 Tau) are categorized into Phase III. Table 2 summarizes basic disk properties for all the targets, showing classification, mass accretion rate, and disk mass. Notably, no clear distinctive properties are observed between Phase I and II sources except for the aforementioned NIR K -band excesses.

We indicate that disks around the intermediate-mass stars necessarily evolve from Phase I to Phase II and, subsequently, to Phase III, while the disks around the low-mass stars evolve from Phase I to Phase III, spending a considerably short time in Phase II (Yasui et al. 2014). It should be noted that H AeBes are categorized into Phase I sources because they are confirmed to contain NIR K -band excesses. Figure 1 plots H Ae stars in a sample used by Cauley & Johns-Krull (2014), whose mass range is roughly comparable to that of our target intermediate-mass stars and whose He I profile morphologies are compared with those of our targets below (Sections 3.4, 3.4, 4.6); the stars are shown with gray squares. We used NIR data from 2MASS PSC and rejected four sources (V1578 Cyg, HD 17081, HD 37490, and Z CMA) that do not have an A photometric quality flag for at least one band in the catalog. Thus, we confirmed that all sources, except for one source, are located in the disk excess region having large color excesses. The exception is HD 141569 ($(J - H, H - K) = (0.01, 0.04)$), which Cauley & Johns-Krull (2014)

categorized into potentially misclassified objects and did not include in their final discussion by indicating that it may not be a H Ae star. Figure 1 also shows the intermediate-mass stars in samples reported by Folha & Emerson (2001) and Edwards et al. (2006) that satisfy the conditions for selecting intermediate-mass stars in Taurus, but are excluded from the sample used in this study because of the limited instrumental sensitivities. They are six sources, and their properties are summarized in Table 3. Four of these sources (CW Tau, GM Aur, DR Tau, and DS Tau) are included in both the previous studies, while HP Tau and HN Tau are included in only one of these references (Folha & Emerson 2001 and Edwards et al. 2006). CW Tau, HP Tau, DR Tau, and HN Tau are categorized into Phase I based on their NIR and MIR excesses, while GM Aur and DS Tau are categorized into Phase II. For reference, CTTSs and weak T Tauri stars (WTTs) are almost comparable to Phase I and Phase III, respectively, in case of low-mass stars (Yasui et al. 2014).

2.2. WINERED Spectroscopy and Data Reduction

We obtained the spectra of selected targets using the NIR spectrograph WINERED (Kondo et al. 2015; Ikeda et al. 2016), attached to the Araki 1.3 m telescope at Koyama Astronomical Observatory, Kyoto-Sangyo University, Japan (Yoshikawa et al. 2012). WINERED has a $1.7 \mu\text{m}$ cutoff 2048×2048 HAWAII-2RG infrared array with a pixel scale of $0''.8 \text{ pixel}^{-1}$, simultaneously covering the wavelength range of $0.91\text{--}1.35 \mu\text{m}$. We used a $1''.65$ width slit, corresponding to 2 pixels, which provides a spectral resolving power of $R = 28,300$ or 11 km s^{-1} . Observations were performed during the following three periods: 2013 February to March; 2013 November to 2014 January; and 2014 September to October. Seeing was typically $\sim 5''$. To avoid saturation in the emission lines, the exposure time for each frame was set to a duration ranging from 300 to 1200 s. Four to twelve sets of data were obtained for each target, resulting in a total exposure time of 1200–7200 s for each target. As the telluric standard stars, the spectra of bright stars with spectral types of late B to early A (B9–A2) at similar airmass ($\Delta \sec z \lesssim 0.2$) were obtained in a similar fashion within 2 hr of target data acquisition on the same night. As the sole exception, the spectra of an MIII spectral type star, HD 1041, as the telluric standard star were obtained for HP Tau/G2. We summarize the details of the observation in Table 4.

All the data were reduced by following the standard procedures using IRAF, including nodding sky subtraction, dome flat-fielding, and aperture extraction. The argon lamp spectra that were obtained at the end of the observing night were used to perform vacuum wavelength calibration. Each target spectrum was divided by the spectrum of the standard star to correct for atmospheric absorption and instrumental response after the photospheric features of the standard spectrum were eliminated (Sameshima et al. 2018). For each echelle order, the spectra were normalized to 1.0. For the continuum level at $\lambda \sim 12700 \text{ \AA}$, where there are no strong photospheric features in synthetic spectra (see Section 3.2) for all the targets, the estimated S/N were ~ 30 to 110 (see Table 4 for each target). The spectra around $P\delta$, $P\gamma$, $P\beta$, and He I (orders of $m = 56, 51, 44,$ and 52 , respectively), reduced by following the above procedure, are depicted for all the targets with respect to the stellar velocities in Figure 2. The spectra are sorted by spectral type from early to late type.

Table 2
Disk Properties of Target YSOs

Object	Phase	SED	C/WTTS	i (deg.)	\dot{M} ($10^{-8} M_{\odot} \text{ yr}^{-1}$)	M_{disk} (M_{\odot})
(1)	(2)	(3)	(4)	(5)	(6)	(7)
V892 Tau	I	II	W	60 (Mo08), 59 (Ha10)	10.5 (DNB18), 7.2 (Liu11)	0.009
AB Aur	I	II	C	<45 (Gr99), 22 (Co05), 40 (Ta12)	14.1 (GNTH06), 1.8 (DB11), 39 (DNB18)	0.004
IRAS 04101+3103	I	II	C
HP Tau/G2	III	III	W	50 (We87), 67 (Bo95)
RY Tau	II	II	C	86 (Mu03), 66 (Is10)	6.4–9.2 (Ca04)	0.02
SU Aur	II	II	C	62 (Ak02), 86 (Mu03)	0.5–0.6 (Ca04)	0.0009
HD 283572	III	III	W	35 (St98), 48 (Wi02), 60 (JBB94)	...	<0.0004
T Tau	I	II	C	19 (HRB97), 20 (Ar02)	3.1–5.7 (Ca04), 3.2 (WG01)	0.008
HBC 388	III	III	W	45 (Ar02)	<0.9 (WG01)	<0.0003
RW Aur	II	II	C	40 (Ar02)	2.0 (In13)	0.004
V773 Tau	II	II	W	34 (Si16)	0.15 (Si16)	0.0005
V410 Tau	III	III	W	54 (Ha95), 70 (JBM94, St94, RS96), 80 (He89), 90 (Bo95)	<0.16 (WG01)	<0.0004
UX Tau	II	II	C	35 (An11)	1.1 (Es10)	0.005

Note. Column (2): phase of the dust disk (Phase I, II, or III) from Yasui et al. (2014; see Section 2.1). Column (3): SED classification type (Class I, II, or III). Column (4): accretion-based classification type (CTTS or WTTS). Column (5): inclination angles. Note that the angles for Phase III sources are often estimated with stellar rotation periods and stellar rotational velocities, while those for Phase I and II sources are estimated from observations of their disks. Column (6): mass accretion rate. Column (7): dust disk masses derived by Andrews & Williams (2005).

References. Mo08: Monnier et al. (2008), Ha10: Hamidouche (2010), DNB18: Dong et al. (2018), Liu11: Liu et al. (2011), Gr99: Grady et al. (1999), Co05: Corder et al. (2005), Ta12: Tang et al. (2012), GNTH06: Garcia Lopez et al. (2006), DB11: Donehew & Brittain (2011), We87: Weaver (1987), Bo95: Bouvier et al. (1995), Mu03: Muzerolle et al. (2003), Is10: Isella et al. (2010), Ca04: Calvet et al. (2004), Ak02: Akeson et al. (2002), St98: Strassmeier et al. (1998), Wi02: Wittkowski et al. (2002), JBB94: Joncour et al. (1994a), HRB97: Herbst et al. (1997), Ar02: Ardila et al. (2002), WG01: White & Ghez (2001), In13: Ingleby et al. (2013), Si16: Simon et al. (2016), Ha95: Hatzes (1995), JBM94: Joncour et al. (1994b), St94: Strassmeier (1994), RS96: Rice & Strassmeier (1996), He89: Herbst (1989), An11: Andrews et al. (2011), Es10: Espaillat et al. (2010).

Table 3
Intermediate-mass Stars in the Samples of Previous Studies (Folha & Emerson 2001; Edwards et al. 2006), and Their Properties

Object	SpT	Phase	$P\beta$ ($P\gamma$)			He I		
			Data	Group	Abs. Type	Data	Group	Abs. Type
(1)	(2)	(3)	(4)	(5)	(6)	(7)	(8)	(9)
CW Tau	K3	I	✓ (✓)	DP (E)	... (...)	✓	DP	...
HP Tau	K3	I	✓	IPC	r			
GM Aur	K3	II	✓ (✓)	IPC (F)	r (...)	✓	F	...
DR Tau	K5	I	✓ (✓)	DP (IPC)	...(r)	✓	PC	b
DS Tau	K5	II	✓ (✓)	IPC (IPC)	r (r)	✓	BR	b, r
HN Tau	K5	I	(✓)	(E)	(...)	✓	DP	...

Note. Column (2): spectral types from Furlan et al. (2006, 2011). Column (3): phase of dust disk (Phase I, II, or III) from Yasui et al. (2014; see Section 2.1). Columns (4)–(6): properties of the $P\beta$ line profiles with those of $P\gamma$ profiles (shown in parentheses). The tick marks in Column 4 mean that the corresponding spectra are available in Folha & Emerson (2001) for $P\beta$ and in Edwards et al. (2006) for $P\gamma$. Column (5): morphology groups based on the classification scheme in Section 3.3. Column (6): type of subcontinuum absorption (blue, red, or centered subcontinuum absorption, denoted by b, r, and c, respectively). Columns (7)–(9): properties of He I line profiles; the tick marks in Column 7 indicate that the corresponding spectra are available in Edwards et al. (2006). Column (8): morphology groups based on the classification scheme in Section 3.3. Column (9): type of subcontinuum absorption (blue, red, or centered subcontinuum absorption, denoted by b, r, and c, respectively).

3. Results

The obtained spectra depict several lines, including those of hydrogen (Paschen series), He I, and metals (e.g., Fe I, Si I, and Mg I). We focus on hydrogen lines and He I $\lambda 10830$ in this study because they are very sensitive to magnetospheric mass accretion and winds.

3.1. Hydrogen Paschen Series

The WINERED wavelength range ($\lambda = 0.91\text{--}1.35 \mu\text{m}$) covers four hydrogen lines: $P\epsilon$ ($\lambda = 9549 \text{ \AA}$), $P\delta$ ($\lambda = 10052 \text{ \AA}$), $P\gamma$ ($\lambda = 10941 \text{ \AA}$), and $P\beta$ ($\lambda = 12822 \text{ \AA}$), where the numbers in

parentheses refer to the vacuum wavelengths. The spectra of $P\delta$, $P\gamma$, and $P\beta$ are depicted in Figure 2 (panels a, b, and d, respectively). Although each spectrum appears to show similar features across various targets, the S/Ns of the spectra are higher at longer wavelengths, resulting in the features of those spectra becoming more prominent. These tendencies are clearly observed in, e.g., RY Tau, SU Aur, UX Tau, and HP Tau/G2. Consider UX Tau as an example. Although the $P\gamma$ spectrum shown in Edwards et al. (2006) exhibits no features, the $P\alpha\beta$ spectrum in Figure 2 depicts significant features, including double peaks with centered subcontinuum absorption, thereby making the diagnostics of magnetospheric accretion possible.

Table 4
Summary of WINERED Observations

Object	Obs Date (YYYY MM DD)	Airmass (sec z)	Exp Time (s)	S/N ^a	Standard ^b
V892 Tau	2013 Dec 8	1.0–1.1	4800 (600 × 8)	58	HR 104 (A2Vs)
AB Aur	2013 Feb 22	1.2	1200 (300 × 4)	82	HIP53910 (A1V)
IRAS 04101+3103	2014 Sep 28	1.1–1.2	3000 (300 × 10)	59	HR 196 (A2Vs)
HP Tau/G2	2013 Dec 4	1.0	2400 (600 × 4)	54	HD 1041 (M1III)
RY Tau	2013 Feb 23	1.3–1.4	1200 (300 × 4)	43	HIP58001 (A0Ve+K2V)
	2013 Feb 23	1.5–1.8	1200 (300 × 4)		HIP23179 (A1V)
SU Aur	2013 Mar 3	1.8–2.5	1800 (300 × 6)	34	HIP76267 (A0V)
HD 283572	2013 Nov 30	1.0	2400 (600 × 4)	113	omi Aur (A2Vp)
T Tau	2013 Dec 2	1.2–1.3	7200 (1200 × 6)	94	HR 196 (A2Vs)
HBC 388	2014 Oct 15	1.2–1.3	2400 (600 × 4)	84	HR 922 (B9V)
RW Aur	2013 Dec 3	1.0	4800 (600 × 8)	55	HR1736 (A2V)
V773 Tau	2013 Nov 28	1.0–1.1	5400 (600 × 9)	74	50 Cas (A2V)
V410 Tau	2013 Dec 8	1.1–1.3	3600 (600 × 6)	33	HR 104 (A2Vs)
UX Tau	2013 Dec 12	1.3	7200 (600 × 12)	37	50 Cas (A2V)

Notes.

^a The pixel-to-pixel S/N of the continuum level at $\lambda \sim 12700 \text{ \AA}$. For RY Tau, the value (43) is from combined spectra of all eight frames.

^b Standard stars used for telluric correction. The spectral type for each standard star is shown in parentheses.

Therefore, we focus on the spectra of $P\beta$ in four lines in the hydrogen Paschen series in this study. This approach can help us to detect the possible characteristics of profile morphologies in different evolutionary phases.

3.2. Removal of Photospheric Features: Estimation of Line Broadening, Radial Velocities, and Veilings

The observed spectra comprise circumstellar and photospheric features. To extract the circumstellar features, it is necessary to eliminate the photospheric features. The photospheric features are broadened (line broadening, v_{broad}), and shifted because of radial velocities (RVs); furthermore, they also exhibit continuum excesses. The excess can be referred to as “veiling,” which is defined as the ratio of the excess emission to the underlying stellar photosphere (see Hartigan et al. 1989). We eliminate the photospheric features using the following procedure. First, by comparing the observed spectra with the synthetic spectra, the stellar properties, line broadenings, RVs, and veilings can be obtained. We further obtain the circumstellar features by subtracting the synthetic spectra from the observed spectra by considering the aforementioned stellar properties.

For each object, we constructed the synthetic spectra using the analysis program SPTOOL (Takeda 1995; Takeda & Kawanomoto 2005), which is based on the ATLAS9 programs from Kurucz (1993). We adopted the metal line list in Meléndez & Barbuy (1999) and the molecular lines from the Vienna Atomic Line Database (VALD3; Ryabchikova et al. 2015). Furthermore, we assumed solar abundance and spectral type from the literature (see Table 1). The adopted parameters for the synthetic spectra, effective temperature (T_{eff}), surface gravity ($\log g$), and microturbulent velocity are provided below. The effective temperatures were adopted from Gray (2005; Table B.1. in Appendix B). When the spectral types for targets were not listed in Gray (2005), close spectral types were used (see Table 5, Column (2)). The $\log g$ was calculated with T_{eff} , stellar mass (M_*), and stellar luminosity (L_*). Because the model dependence of $\log g$ is considered to be very small (Takagi et al. 2011), we used the values of T_{eff} , M_* , and L_*

from a PMS isochrone model, Siess et al. (2000), by considering the age of Taurus (1.5 Myr old). The obtained $\log g$ values are 4.1 for spectral type B8, 3.5 for spectral type K0, and 3.7 for spectral types K3–K5. We adopted the values of 4.1 for late-B to early-A type stars (V892 Tau, AB Aur, and IRAS 04101+3103), 3.5 for G0–K1 type stars (HP Tau/G2, RY Tau, SU Aur, HD 283572, T Tau, and HBC 388), and 3.7 for K3–K5 type stars (RW Aur, V773 Tau, V410 Tau, and UX Tau). For microturbulent velocity, we adopted 2 km s^{-1} following Gray et al. (2001), who observed a tight correlation between microturbulence and $\log g$ in the spectral range of late-A to early-G type (see Figure 7 in Gray et al. 2001).

We derived line broadening v_{broad} , RV, and Y - and J -band veilings (γ_Y and γ_J , respectively) for each target by fitting the obtained synthetic spectra with the observed spectra. First, we roughly estimated v_{broad} ¹¹ and RV by fitting the obtained synthetic spectra with the observed spectra using the automatic profile-fitting program MPFIT (Takeda 1995) included in SPTOOL. Note that the veilings are not yet considered at this stage. Among the spectra shown in Figure 2 ($m = 56, 52, 51$, and 44), our fitting procedure used spectra with interference order $m = 52$, which included He I $\lambda 10830$, because these spectra show a large number of relatively deep lines, with normalized counts of less than 0.7 in normalized synthetic spectra at $v_{\text{broad}} = 0 \text{ km s}^{-1}$. The deep lines used for the fitting, in the wavelength ranges of $\lambda = 10710\text{--}10815 \text{ \AA}$ and $10855\text{--}10875 \text{ \AA}$, are not affected by the He I $\lambda 10830$ features and do not include data with very low S/N due to the edges of the spectra. The lines used for the stars with spectral types G–K2 were Si I ($\lambda 10730.3, 10752.3, 10787.5, 10789.8, 10871.8, 10872.5$), Mg I $\lambda 10814.1$, and C I $\lambda 10732.5$. For stars with spectral type of K3 or later, the Fe I lines ($\lambda 10756.0, 10786.0$) were used in addition to the above lines; however, C I was not used because it was weak in case of later-type stars. We further derived v_{broad} , RVs, and γ_Y by comparing several synthetic spectra. The best fit was determined

¹¹ Here, v_{broad} is parameterized by FWHM. However, because the output velocity in MPFIT is a convolution of v_{broad} and the instrumental broadening, and because it is parameterized by the e -folding half width, it is converted into v_{broad} according to Takeda et al. (2008).

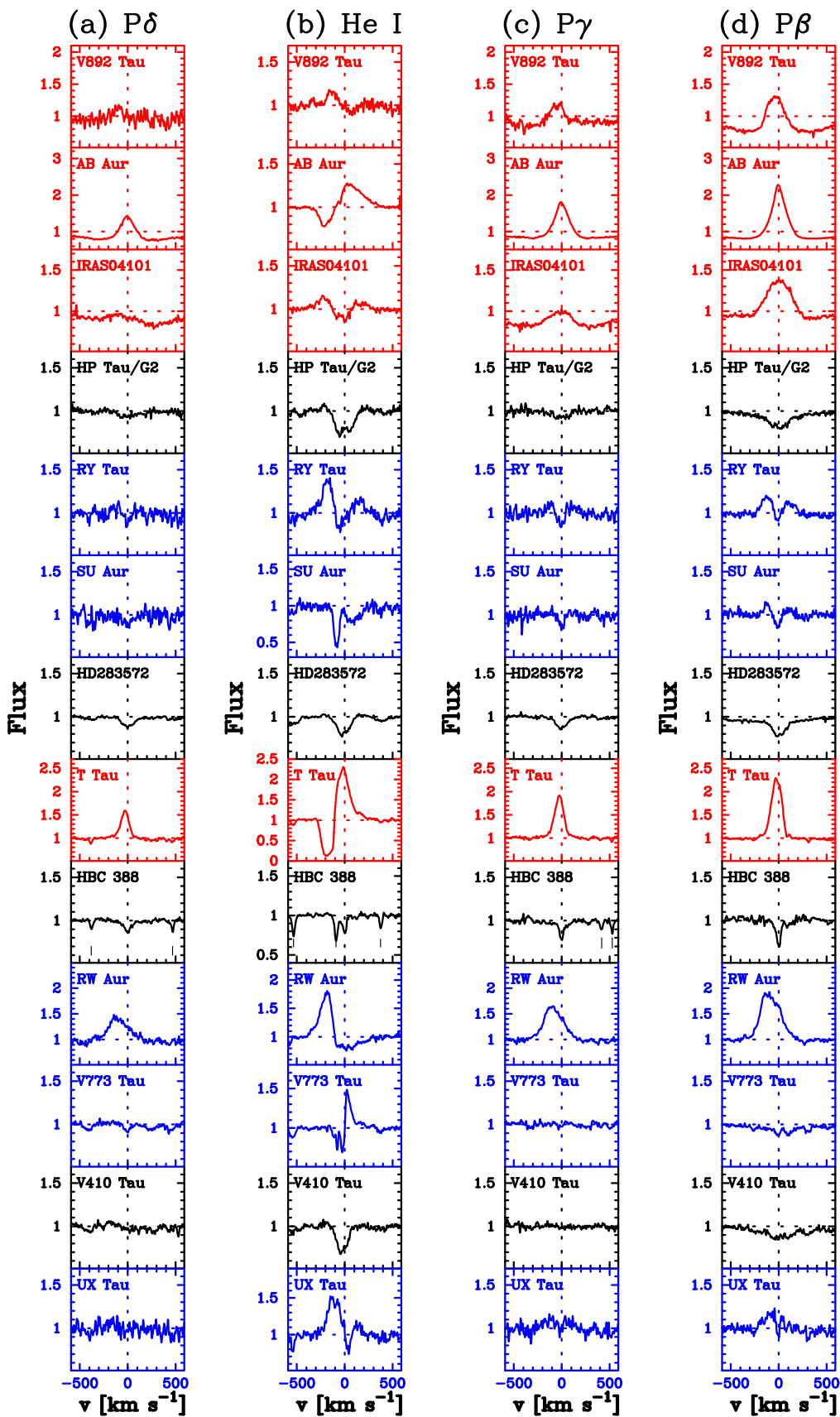


Figure 2. Spectral regions of $P\delta$ (a), $\text{He I } \lambda 10830$ (b), $P\gamma$ (c), and $P\beta$ (d). Fluxes are normalized to the continuum. Velocities are relative to the stellar rest velocities. The spectra are sorted by spectral type, from early to late type. Spectra for Phase I, II, and III sources are shown with red, blue, and black, respectively. Photospheric features are marked with vertical lines in the panels for HBC 388. Note that the plot range has been widened for some objects with strong features.

Table 5
Obtained Properties from the Fit of the Synthetic Spectra

Object	SpT	v_{broad} (km s^{-1})	RV (km s^{-1})	γ_Y	γ_J
(1)	(2)	(3)	(4)	(5)	(6)
V892 Tau	A0 (B9)	(100 (a))	(16.0 (b))
AB Aur	A0 (A0)	(116 (c))	(24.7 (c))
IRAS 04101+3103	A0 (A1)	(100)	(20)
HP Tau/G2	G0 (G0)	120	15.1	0.1	0.1
RY Tau	G0 (G1)	65	22.9	0.4	0.3
SU Aur	G0 (G1)	85	23.9	0.3	0.2
HD 283572	G5 (G5)	105	17.9	0.0	0.1
T Tau	K0 (K0)	35	21.8	0.9	0.5
HBC 388	K0 (K1)	25	15.7	0.0	0.0
RW Aur	K3 (K3)	35	13.5	1.0	0.2
V773 Tau	K3 (K3)	60	5.6	0.4	0.3
V410 Tau	K3 (K3)	130	26.2	0.0	0.0
UX Tau	K5 (K5)	25	12.5	0.6	1.0

Note. Column (2): spectral types of target objects used for synthetic spectra. Spectral types from the literature are shown in parentheses. Column (3): line broadening measured in velocity units. For V892 Tau and AB Aur, values from the literature are assumed and are shown in parentheses. For IRAS 04101+3103, 100 km s^{-1} is assumed, shown in parentheses (see more detail in the main text). Column (4): radial velocities. For V892 Tau and AB Aur, values from the literature are assumed. For IRAS 04101+3103, the average RV value for all targets, 20 km s^{-1} , is assumed (see more detail in the main text). Column (5): Y -band veiling. Column (6): J -band veiling.

References. (a) Mooley et al. (2013). (b) Bertout & Genova (2006). (c) Alecian et al. (2013).

using the minimum chi-squared value by varying the three parameters of v_{broad} , RV, and γ_Y . The synthetic spectra were constructed using the following limits on each parameter: (1) v_{broad} values around initially estimated values with 5 km s^{-1} step; (2) γ_Y values in the range of 0.0–2.0 with 0.1 step; and (3) observed spectra with wavelength shifts for RVs with 0.1 \AA step. For the fitting, the same wavelength range was used as was used in the initial estimate of v_{broad} . When estimating v_{broad} and RV, we also estimated γ_J using spectra with order $m = 44$ in the same way as the derivation of γ_Y , but in the spectral range of 12620–12700 \AA using lines of Fe I $\lambda 12642.2$, Fe I $\lambda 12652.2$, and Na I $\lambda 12682.7$. The obtained properties (v_{broad} , RV, γ_Y , and γ_J) are summarized in Table 5. Finally, we obtained residual profiles of $P\beta$ and He I by subtracting synthetic spectra considering the obtained properties from observed spectra. The profiles relative to the stellar rest velocities are shown in Figure 3.

We note that we could not estimate v_{broad} , RV, and veilings using the above procedure for three early-type stars with spectral types of late B to early A: V892 Tau, AB Aur, and IRAS 0401+3103. This was due to a lack of prominent photospheric features in their spectra except for H I. There are only a small number of photospheric features in the spectra for such early-type stars, and even the existing features become quite broadened and very shallow due to the large rotation velocities (e.g., $v \sin i = 116 \text{ km s}^{-1}$ for AB Aur; 100 km s^{-1} for V892 Tau). Instead, we used synthetic spectra assuming v_{broad} and RV values from the literature, without considering veilings ($\gamma_Y = 0$, $\gamma_J = 0$), for the subtraction of photospheric features from the observed spectra. As for v_{broad} of AB Aur, only the projected rotation velocity ($v \sin i$) was provided by the literature (Alejian et al. 2013), $v \sin i = 100 \text{ km s}^{-1}$. Nonetheless, we had to input v_{broad} , using combinations of $v \sin i$ and macroturbulence

velocity (v_{mac}), when making synthetic spectra with SPTOOL. Alecian et al. (2013) assumed a v_{mac} of 2 km s^{-1} , and suggested that in the case that $v \sin i$ is higher than 40 km s^{-1} , v_{mac} is not a significant parameter. Therefore, we adopted their $v \sin i$ values for v_{broad} . Also, for the v_{broad} value for V892 Tau, only $v \sin i$ (116 km s^{-1}) was provided by the literature (Mooley et al. 2013). Although we could not find the adopted value of v_{mac} , it should be negligible for v_{broad} , considering the large $v \sin i$ value. Therefore, we adopted this value as v_{broad} . However, we could not find any literature references for the v_{broad} and RV values for IRAS 04101+3103. We adopted the average value of RVs for all target objects in this paper (Table 1, Column (9)) that all exist in the Taurus star-forming region, $\sim 20 \text{ km s}^{-1}$. For v_{broad} , we assumed a value of 100 km s^{-1} , similar to the values for AB Aur and V892 Tau, considering that their spectral types are almost the same and their disk evolutionary phases are the same (Phase I). As for veilings, we could not find any references about veilings for these three sources. Because the photospheric He I lines show prominent features only in very early-type stars, $\sim B5$ and earlier (Cauley & Johns-Krull 2014), which are not included in our targets, variations of synthetic spectra have little impact on our residual profiles. However, because photospheric $P\beta$ lines show very prominent absorption features in late-B and early-A type stars (our early-type targets), differences between photospheric features in assumed synthetic spectra and those in actual spectra may have a great impact on the residual profiles in normalization. We discuss the possible impact of assuming zero veilings on obtained residual profiles in Section 3.3.

Estimated v_{broad} , RV, γ_Y , and γ_J values for each target are summarized in Table 5. WTTs, comparable to Phase III objects in this paper, are known to show no veiling (e.g., Edwards et al. 2006), while a correlation between mass accretion rate and veiling for CTTSs has been suggested (e.g., Beristain et al. 2001). For all four Phase III objects (HP Tau/G2, HD 283572, HBC 388, and V410 Tau), γ_Y and γ_J are estimated to be almost zero although some estimated values are nonzero ($\gamma_Y = \gamma_J = 0.1$ for HP Tau/G2; $\gamma_J = 0.1$ for HD 283572). Therefore, taking all results of Phase III objects into an account, the estimated veilings are ≤ 0.1 , suggesting that veilings are accurately estimated with uncertainties of ~ 0.1 .

3.3. $P\beta$ Line Profiles

Paschen line emissions are thought to arise primarily in the magnetospheric accretion column (Hartmann et al. 2016). Although the profiles of the Paschen lines in the spectra we obtained ($P\epsilon$, $P\gamma$, $P\delta$, and $P\beta$) show similar morphologies, we discuss those of $P\beta$, which show the most prominent features, as discussed in Section 3.1. In this section, we focus on the properties of the $P\beta$ emission for each source. We discuss the implications for the profile morphology in Section 4.

We detected $P\beta$ in 8 of our 13 targets (all Phase I sources, and all Phase II sources except for V773 Tau), while these lines are not detected in 5 sources (V773 Tau and all Phase III sources). The detection rates for Phase I, II, and III objects are 100% (4/4), 80% (4/5), and 0% (0/4), respectively. In Table 6 we summarize the $P\beta$ profile parameters obtained from the residual profiles (Figure 3), showing the object name in Column (1), profile type in Column (2), the maximum blueshifted and redshifted line velocities ($V_{\text{max}}^{\text{blue}}$ and $V_{\text{max}}^{\text{red}}$) in Columns (3) and (4), the velocity of peak emission and absorption ($V_{\text{peak}}^{\text{em}}$ and $V_{\text{peak}}^{\text{abs}}$) in Columns (5) and (6), the line fluxes relative to the continuum at the peak emission and

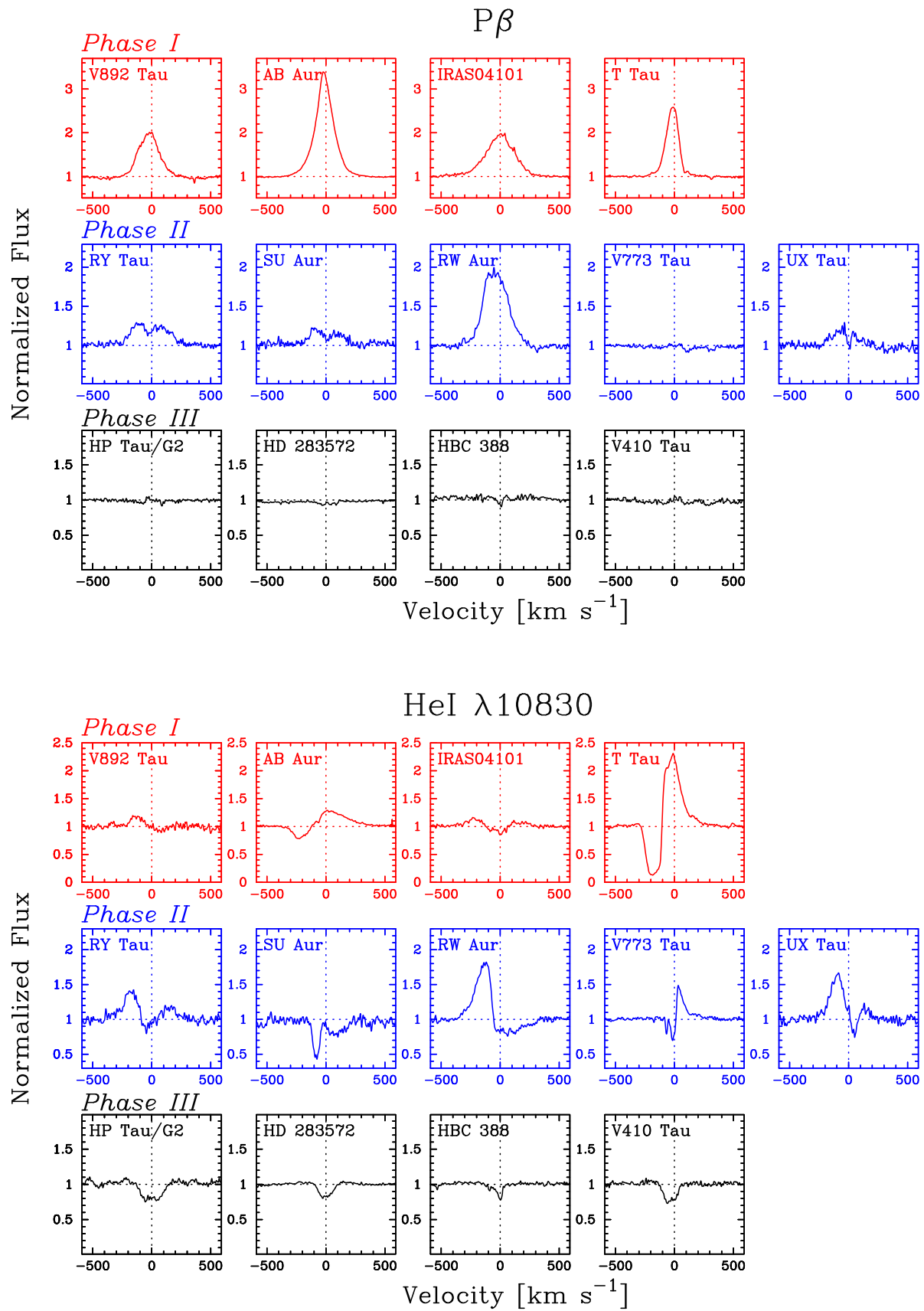


Figure 3. Residual $P\beta$ profiles (top) and He I profiles (bottom). Velocities are relative to the stellar rest velocities. Spectra for Phase I, II, and III sources are shown in top, middle, and bottom panels, respectively.

Table 6
P β Profile Parameters

Object	Profile Type	V_{\max}^{blue} (km s^{-1})	V_{\max}^{red} (km s^{-1})	$V_{\text{peak}}^{\text{em}}$ (km s^{-1})	$V_{\text{peak}}^{\text{abs}}$ (km s^{-1})	$F_{\text{peak}}^{\text{em}}$	$F_{\text{peak}}^{\text{abs}}$	Em. W_{λ} (\AA)	Ab. W_{λ} (\AA)	Ab. Type
(1)	(2)	(3)	(4)	(5)	(6)	(7)	(8)	(9)	(10)	(11)
V892 Tau	E	−350 (−250)	250 (200)	−20	...	2.01 (1.64)	...	8.93 (5.74)
AB Aur	E	−400 (−350)	400 (300)	−20	...	3.39 (2.69)	...	19.0 (13.1)
IRAS 04101+3103	E	−500 (−350)	400 (350)	5	...	1.98 (1.57)	...	12.2 (7.2)
HP Tau/G2	F
RY Tau	DP	−400	300	−100	...	1.27	...	4.00
SU Aur	DP	−300	250	−100	...	1.22	...	2.29
HD 283572	F
T Tau	E	−250	250	−15	...	2.56	...	9.15
HBC 388	F
RW Aur	IPC	−400	450	−50	305	1.99	0.96	10.36	0.20	r
V773 Tau	F
V410 Tau	F
UX Tau	DP	−250	250	−35	...	1.29	...	1.68

Note. Column (2): profile type based on classification scheme in Section 3.3 (see main text for details). Columns (3) and (4): the maximum blueshifted and redshifted line velocities. For V892 Tau, AB Aur, and IRAS 04101+3103, estimated values assuming $\gamma_Y = \gamma_J = 0.0$ are shown, while those assuming $\gamma_Y = 2.0$, $\gamma_J = 2.0$ are shown in parentheses. Columns (5) and (6): velocity of peak emission and absorption. Columns (7) and (8): line fluxes relative to the continuum at the peak emission and absorption velocities. Columns (9) and (10): emission and absorption EWs. Column (11): type of subcontinuum absorption: blue, red, or centered subcontinuum absorption are marked by the letter b, r, and c, respectively.

absorption velocities ($F_{\text{peak}}^{\text{em}}$ and $F_{\text{peak}}^{\text{abs}}$) in Columns (7) and (8), emission and absorption EWs (Em. W_{λ} and Ab. W_{λ}) in Columns (9) and (10), and the type of subcontinuum absorption in Column (11). In Column 2 we categorize residual spectra into morphology groups based on the classification scheme of Cauley & Johns-Krull (2014). They divided the line profiles into six groups: (1) P Cygni (PC), (2) inverse P Cygni (IPC), (3) pure absorption (A), (4) single-peaked emission (E), (5) double-peaked emission (DP), and (6) featureless (F). We added a new category, a profile with both blueshifted and redshifted subcontinuum absorption, but with zero or one emission peak (hereafter, “BR”). Reipurth et al. (1996) have reported another well-known classification. The groups E, PC, and IPC in the classification by Cauley & Johns-Krull (2014) correspond to type I, type IV B, and type IV R in the classification of Reipurth et al. (1996), respectively, and group DP by Cauley & Johns-Krull (2014) comprises type II and type III of Reipurth et al. (1996).

The P β profiles for the targets are categorized into the following four groups: group E, group DP, group IPC, and group F. The profiles of all the four Phase I sources (V892 Tau, AB Aur, IRAS 04101+3103, and T Tau) are categorized into group E. They all exhibit approximately symmetric and broad features with $|V_{\text{peak}}^{\text{em}}| \leq 20 \text{ km s}^{-1}$ for all the sources, and $|V_{\text{max}}^{\text{blue}}|$ and $|V_{\text{max}}^{\text{red}}|$ of $\gtrsim 300 \text{ km s}^{-1}$ except for T Tau ($|V_{\text{max}}| \sim 250 \text{ km s}^{-1}$). They have slightly redward absorption features judging from the $|V_{\text{max}}^{\text{blue}}|$ values, which exceed $|V_{\text{max}}^{\text{red}}|$ by $\sim 50 \text{ km s}^{-1}$. In addition, the profiles of three of the sources (RY Tau, SU Aur, and UX Tau) are categorized into group DP. All the sources in this group are influenced by redward absorption, judging from $V_{\text{peak}}^{\text{em}} < 0$. The profile for UX Tau shows subcontinuum absorption centered on the stellar rest velocity. The profile of RW Aur is categorized into group IPC, which has a very slight subcontinuum feature with $F_{\text{peak}}^{\text{abs}} = 0.96$. Finally, the profiles of the remaining five sources (V773 Tau, HP Tau/G2, HD 283572, HBC 388, and V410 Tau) are categorized into group F.

We note the possibility that photospheric features in P β profiles for A- and B-type stars (V892 Tau, AB Aur, and IRAS 04101+3103) are not completely removed in the residual profiles shown in Figure 3 because there is no information on veilings for the early-type stars and we tentatively adopted synthetic spectra assuming zero veilings as photospheric features (Section 3.2). We checked the variation in the residual profiles we obtained, assuming the extreme case of high veilings, 2.0, as shown in Table 6 in parentheses. As a result, we found that variations are $\sim 100 \text{ km s}^{-1}$. Although the variations are very large, their impacts are negligible because the interpretation of the profile is only based on line morphology and not on line width or intensity (Section 4.2).

3.4. He I $\lambda 10830$ Line Profiles

He I $\lambda 10830$ line emissions are thought to have a composite origin, including contributions from wind, from the funnel flow, and from an accretion shock (Edwards et al. 2006). In this section, we focus on the properties of He I emission for each source. We discuss the implication of the profile morphology in Section 4.

We detect He I $\lambda 10830$ features with absorption below the continuum in all of our targets. The detection rates of He I lines for Phase I, II, and III objects are 100% (4/4), 100% (5/5), and 100% (4/4), respectively. In Table 7 we summarize the He I profile parameters that are obtained from residual profiles in Figure 3, in the same manner as for the P β profile parameters in Section 3.3. In Column (2), we categorize He I residual spectra into morphology groups in Section 3.3.

The He I profiles for the targets are categorized into five groups, group IPC, group PC, group DP, group BR, and group A. The profiles of two sources (V892 Tau and RW Aur) are categorized into group IPC; both exhibit broad features with $|V_{\text{max}}^{\text{blue}}|$ and $|V_{\text{max}}^{\text{red}}|$ of $\gtrsim 250 \text{ km s}^{-1}$. The profiles of three of the sources (AB Aur, T Tau, and V773 Tau) are categorized into group PC; the profiles of AB Aur and T Tau exhibit broad features with $|V_{\text{max}}^{\text{blue}}|$ and $|V_{\text{max}}^{\text{red}}| \gtrsim 250 \text{ km s}^{-1}$, while that of

Table 7
He I Profile Parameters

Object	Profile Type	V_{\max}^{blue} (km s^{-1})	V_{\max}^{red} (km s^{-1})	$V_{\text{peak}}^{\text{em}}$ (km s^{-1})	$V_{\text{peak}}^{\text{abs}}$ (km s^{-1})	$F_{\text{peak}}^{\text{em}}$	$F_{\text{peak}}^{\text{abs}}$	Em. W (\AA)	Ab. W (\AA)	Ab. Type
(1)	(2)	(3)	(4)	(5)	(6)	(7)	(8)	(9)	(10)	(11)
V892 Tau	IPC	-250	200	-155	80	1.19	0.88	0.18	0.09	r
AB Aur	PC	-400	400	45	-225	1.29	0.79	2.71	0.98	b
IRAS 04101+3103	DP	-450	350	-230	0	1.16	0.85	1.12	0.48	c
HP Tau/G2	A	-150	150	...	~ 0	...	0.75	...	1.50	c
RY Tau	DP	-400	300	-155	-40	1.41	0.79	3.03	0.32	b
SU Aur	BR	-200	250	...	-95	...	0.47	...	2.32	b, r
HD 283572	A	-100	100	...	~ 0	...	0.83	...	0.82	c
T Tau	PC	-300	400	-10	-185	2.31	0.13	7.47	3.98	b
HBC 388	A	-100	50	...	0	...	0.78	...	0.51	c
RW Aur	IPC	-400	350	-140	60	1.81	0.76	4.32	1.73	r
V773 Tau	PC	-100	250	30	-15	1.49	0.70	1.32	0.44	b
V410 Tau	A	-160	120	...	~ 0	...	0.69	...	1.06	c
UX Tau	DP	-300	250	-85	50	1.71	0.74	3.69	0.33	r

Note. Column (1): object name. Column (2): profile type based on classification scheme in Section 3.3 (see main text for details). Columns (3) and (4): maximum blueshifted and redshifted line velocities. Columns (5) and (6): velocity of peak emission and absorption. Columns (7) and (8): line fluxes relative to the continuum at the peak emission and absorption velocities. Columns (9) and (10): emission and absorption EWs. Column (11): type of subcontinuum absorption: blue, red, or centered subcontinuum absorption are marked by the letter b, r, and c, respectively.

V773 Tau has relatively narrow features with $|V_{\max}^{\text{blue}}|$ and $|V_{\max}^{\text{red}}| \lesssim 250 \text{ km s}^{-1}$. The profiles of three of the sources (IRAS 04101+3101, RY Tau, and UX Aur) are categorized into group DP; they exhibit broad features with $|V_{\max}^{\text{blue}}|$ and $|V_{\max}^{\text{red}}|$ of $\gtrsim 250 \text{ km s}^{-1}$. The profiles of all the four Phase III sources (HP Tau/G2, HD 283572, HBC 388, and V410 Tau) are considered to be group A; they demonstrate centered subcontinuum and exhibit narrow profiles with $|V_{\max}^{\text{blue}}|$ and $|V_{\max}^{\text{red}}|$ of $\lesssim 150 \text{ km s}^{-1}$. The profile of SU Aur is assigned to a new category, group BR; it exhibits redshifted and blueshifted subcontinuum absorption, which is a relatively narrow feature with $|V_{\max}^{\text{blue}}|$ and $|V_{\max}^{\text{red}}| \lesssim 250 \text{ km s}^{-1}$.

4. Discussion

Our WINERED data present a variety of profile morphologies in the $P\beta$ and He I $\lambda 10830$ lines. In this section, the 13 sources observed in this study and the 6 sources observed in previous studies (among them 5 sources each for $P\beta$ and He I; Folha & Emerson 2001; Edwards et al. 2006; see Section 2.1) are considered in combination for obtaining improved statistical accuracy. The statistics of the categorized line profile morphologies (Section 4.1) and the manner in which the profile morphology for each target provides an insight into magnetospheric accretion and inner winds (Section 4.2), and the possible progression of dominant processes through the disk evolutionary phases (Section 4.3) are discussed herein. The suggested progression is compared with previous studies (Section 4.4). The chromospheric activities in Phase III sources from He I profile morphologies are also evaluated (Section 4.5). Finally, the implications of the results are considered for the theories of mass-flow processes (Section 4.6).

4.1. Profile Morphologies

4.1.1. $P\beta$ Line Profile Morphologies

Folha & Emerson (2001) presented the $P\beta$ profiles for five of the six additional stars (CW Tau, HP Tau, GM Aur, DR Tau, and DS Tau). The $P\beta$ line profile morphologies for 18

intermediate-mass stars (the 13 targets observed in the present study and the 5 additional targets observed in previous studies) are considered in combination. Based on the classification scheme in Section 3.3, they are categorized into two groups: two (CW Tau and DR Tau) in group DP, and three (HP Tau, GM Aur, and DS Tau) in group IPC (see Table 3).

The statistics of the $P\beta$ line profile morphologies for 18 intermediate-mass stars for each evolutionary phase are summarized in Table 8. The $P\beta$ line profiles for Phase I sources are categorized into three groups: four (V892 Tau, AB Aur, IRAS 04101+3103, and T Tau) in group E, two (CW Tau and DR Tau) in group DP, and one (HP Tau) in group IPC. The $P\beta$ line profiles for Phase II sources are categorized into three groups: three (RY Tau, SU Aur, and UX Tau) in group DP, three (RW Aur, GM Aur, and DS Tau) in group IPC, and one (V773 Tau) in group F. Finally, the $P\beta$ line profiles of all of the Phase III sources are categorized into group F. The statistics of Phase III are clearly different from those of Phase I and II, while those of Phase I and Phase II do not appear to differ significantly, except for the fact that a large fraction of Phase I sources but none of the Phase II sources are present in group E. Edwards et al. (2006) reported the $P\gamma$ profiles for five sources (CW Tau, GM Aur, DR Tau, DS Tau, and HN Tau) of the six additional sources noted in Section 2.1. The trends observed in these profiles are similar to those in the $P\beta$ profiles, although the $P\gamma$ profile features are sometimes weaker than the $P\beta$ features (Section 3.1): of the Phase I sources, two of which are in group E and one in group IPC, and of the Phase II sources, one of which is in group F and one in group IPC. However, it should be noted that the profile types are not necessarily the same for each source in the $P\beta$ profiles presented by Folha & Emerson (2001) and $P\gamma$ profiles presented by Edwards et al. (2006). Because the spectra of $P\gamma$ and $P\beta$ show similar features across various targets in the same observation period (see Section 3.1), the differences of the profile types can be attributed to the differences in the observation period; this is further discussed in Section 4.3.

We compared the $P\beta$ profile morphologies for intermediate-mass stars and those from previous Paschen line spectroscopic

Table 8
Statistics Summary of $P\beta$ Features

	E	DP	PC	IPC	A	F	BR	Reference
<i>Intermediate-mass stars</i>								
Phase I	57% (4/7)	29% (2/7)	0% (0/7)	14% (1/7)	0% (0/7)	0% (0/7)	0% (0/7)	This study, FE01
Phase II	0% (0/7)	43% (3/7)	0% (0/7)	43% (3/7)	0% (0/7)	14% (1/7)	0% (0/7)	This study, FE01
Phase III	0% (0/4)	0% (0/4)	0% (0/4)	0% (0/4)	0% (0/4)	100% (4/4)	0% (0/4)	This study, FE01
<i>Low-mass stars</i>								
CTTS ^a	49% (20/41)	12% (5/41)	0% (0/41)	32% (13/41)	0% (0/41)	7% (3/41)	0% (0/41)	FE01
WTTS	0% (0/3)	0% (0/3)	0% (0/3)	0% (0/3)	0% (0/3)	100% (3/3)	0% (0/3)	FE01
CTTS ($P\gamma$) ^b	69% (27/39)	3% (1/39)	0% (0/39)	21% (8/39)	0% (0/39)	8% (3/39)	0% (0/39)	Ed06
WTTS ($P\gamma$) ^c	17% (1/6)	0% (0/6)	0% (0/6)	0% (0/6)	0% (0/6)	83% (5/6)	0% (0/6)	Ed06

Notes.

^a The line profiles for 41 CTTSs in the sample of Folha & Emerson (2001) with sufficient S/Ns were used (see main text for details).

^b The $P\beta$ line profiles for all CTTSs except for 12 sources (DR Tau, RW Aur A, DS Tau, YY Ori, AA Tau, GI Tau, CI Tau, BM And, RW Aur B, SU Aur, UX Tau, and GM Aur) are categorized into group E. The line profiles for the 12 sources are as follows: group DP: SU Aur; group IPC: DR Tau, RW Aur A, DS Tau, YY Ori, AA Tau, GI Tau, BM And, and RW Aur B; Group F: CI Tau, UX Tau, and GM Aur.

^c The $P\beta$ line profiles for all WTTSs except for V826 Tau are categorized into group F. Although classification is difficult for V826 Tau due to very subtle features ($W_\lambda < 0.3 \text{ \AA}$), we categorize it into group E.

References. FE01: Folha & Emerson (2001), Ed06: Edwards et al. (2006).

observations of YSOs with high spectral resolution (Folha & Emerson 2001; Edwards et al. 2006). The targets in these studies were primarily low-mass¹² T Tauri stars. Folha & Emerson (2001) presented $P\beta$ line profiles for 49 T Tauri stars (44 CTTSs, 4 WTTSs, and one variable star between CTTS and WTTS). Of these, 45 sources (41 CTTSs, 3 WTTSs, and one variable star between CTTS and WTTS) with sufficient S/Ns are counted later in this paper.¹³ Edwards et al. (2006) presented $P\gamma$ line profiles for 48 T Tauri stars (39 CTTSs, 6 WTTSs, and three Class I sources). Although the observations by Edwards et al. (2006) were not for $P\beta$, the $P\gamma$ morphology of the profile is known to be reminiscent of the $P\beta$ profile (Edwards et al. 2006). Folha & Emerson (2001) detected $P\beta$ emission in 38 of 41 CTTSs in their sample, while Edwards et al. (2006) detected $P\gamma$ emission in 38 of 39 CTTSs in their sample. For profiles of low-mass stars from previous studies, redshifted absorption features are common, while none shows blueshifted absorption features. This is the case for the profiles we obtained for intermediate-mass stars in our sample. For comparison, we show the statistics of the profile morphology of Paschen lines for CTTSs by Folha & Emerson (2001) and Edwards et al. (2006) in Table 8. For both samples, the occurrence rate of group E is highest (~ 50 to 70%). This tendency is similar to that for Phase I sources in the intermediate-mass star sample. Because CTTSs are comparable to Phase I (Section 2.1), this tendency seems to be a natural consequence. The occurrence rate of group IPC sources is the second highest for CTTSs in previous studies conducted by Folha & Emerson (2001) and Edwards et al. (2006), ~ 20 to 30% . This is consistent with those for Phase I and II sources in the intermediate-mass star sample. In contrast, group DP sources are very rare in CTTSs ($\lesssim 10\%$), as suggested by Folha & Emerson (2001), while the occurrence rate is relatively high for Phase I and II sources in the intermediate-mass star sample

($\sim 30\%$ – 40%). This may be characteristic for intermediate-mass stars. However, the statistics of CTTSs do not appear to differ significantly from those of Phase I and II sources in the intermediate-mass star sample. Last, we also show the statistics of profile morphology of Paschen lines for WTTSs, which are comparable to low-mass stars in Phase III, by Folha & Emerson (2001) ($P\beta$) and Edwards et al. (2006) ($P\gamma$) in Table 8. Paschen lines are undetected in almost all WTTSs in Folha & Emerson (2001) and in Edwards et al. (2006), prompting a classification in group F. This result is consistent with those for our target intermediate-mass stars in Phase III.

4.1.2. He I Line Profile Morphologies

For five of the six additional stars, Edwards et al. (2006) reported the He I profiles (CW Tau, GM Aur, DR Tau, DS Tau, and HN Tau). In this section, the He I line profile morphologies for 18 intermediate-mass stars (the 13 targets observed in the present study and the 5 additional targets observed in previous studies) are considered. The sources are categorized into four groups based on the classification scheme in Section 3.3: two (CW Tau and HN Tau) are assigned to group DP, one (GM Aur) is assigned to group F, one (DR Tau) is assigned to group PC, and one (DS Tau) is assigned to group BR (see Table 3).

The statistics of the He I line profile morphologies for the 18 intermediate-mass stars for each evolutionary phase are shown in Table 9. The line profiles of Phase I sources are categorized into three groups: three (AB Aur, T Tau, and DR Tau) are categorized into group PC, three (IRAS 04101+3103, CW Tau, and HN Tau) are in group DP, and one (V892 Tau) is in group IPC. The Phase II sources are categorized into five groups: two (RY Tau and UX Tau) in group DP, two (SU Aur and DS Tau) in group BR, one (RW Aur) in group IPC, one (V773 Tau) in group PC, and one (GM Aur) in group F. Finally, all the Phase III sources are categorized into group A. Based on these statistics, the He I profiles of the sources in Phase I and II are similar to each other, but the profiles of the Phase III sources are clearly different (all in group A) from those in the remaining phases. However, in terms of broadness of spectral features, there seem to be clear differences between

¹² Some of the targets by Folha & Emerson (2001) and Edwards et al. (2006) are the same as ours: V773 Tau, RY Tau, T Tau, SU Aur, and RW Aur in Folha & Emerson (2001); SU Aur, RW Aur, and UX Tau in Edwards et al. (2006).

¹³ Folha & Emerson (2001) pointed out that for some sources, the $P\beta$ lines are too noisy to allow a reliable classification of their profiles: three CTTSs (DQ Tau, FX Tau and GH Tau), and one WTTS (DI Tau).

Table 9
Statistics Summary of He I Features and Blueshifted Absorption Types

	Spectral Type						Blue Abs. Type		Reference	
	E	DP	PC	IPC	A	F	BR	Broad		Narrow
<i>Intermediate-mass stars</i>										
Phase I	0% (0/7)	43% (3/7)	43% (3/7)	14% (1/7)	0% (0/7)	0% (0/7)	0% (0/7)	43% (3/7)	0% (0/7)	This study, Ed06
Phase II	0% (0/7)	29% (2/7)	14% (1/7)	14% (1/7)	0% (0/7)	14% (1/7)	29% (2/7)	0% (0/7)	57% (4/7)	This study, Ed06
Phase III	0% (0/4)	0% (0/4)	0% (0/4)	0% (0/4)	100% (4/4)	0% (0/4)	0% (0/4)	0% (0/4)	0% (0/4)	This study
HAe	7% (2/28)	11% (3/28)	36% (10/28)	32% (9/28)	7% (2/28)	7% (2/28)	0% (0/28)	36 (10/28)	0 (0/28)	CJ14
<i>Low-mass stars</i>										
CTTS ^a	3% (1/39)	21% (8/39)	36% (14/39)	13% (5/39)	0% (0/39)	3% (1/39)	26% (10/39)	38 (15/39)	28 (11/39)	Ed06
WTTS ^b	33% (2/6)	0% (0/6)	0% (0/6)	0% (0/6)	0% (0/6)	67% (4/6)	0% (0/6)	0 (0/6)	0 (0/6)	Ed06

Notes.

^a The line profiles for CTTSs are categorized as follows: group E: BP Tau; group DP: CW Tau, RW Aur A, HN Tau, DS Tau, GK Tau, UZ Tau E, V836 Tau, UX Tau; group PC: DR Tau, AS 353A, DL Tau, HL Tau, DG Tau, DF Tau, DO Tau, GG Tau, GW Ori, DE Tau, DD Tau, DQ Tau, TW Hya, XZ Tau; group IPC: AA Tau, BM And, RW Aur B, LkCa8, DN Tau; group F: GM Aur; group BR: DK Tau, HK Tau, UY Aur, YY Ori, CI Tau, CY Tau, FP Tau, GI Tau, UZ Tau W, SU Aur.
^b The line profiles for all WTTSs except for V826 Tau and TWA 14 are categorized into group F, while those for V826 Tau and TWA 14 are categorized into group E.

Reference: CJ14: Cauley & Johns-Krull (2014); Ed06: Edwards et al. (2006).

Phase I and II sources: all four Phase I sources show broad features with $|V_{\max}^{\text{blue}}|$ or $|V_{\max}^{\text{red}}|$ of $\gtrsim 250 \text{ km s}^{-1}$, while some Phase II sources (SU Aur and V773 Tau) show narrow features with $|V_{\max}^{\text{blue}}|$ or $|V_{\max}^{\text{red}}|$ of $\lesssim 250 \text{ km s}^{-1}$.

We compare He I $\lambda 10830$ profile morphologies for intermediate-mass stars with those from previous He I spectroscopic observations of YSOs with high spectral resolution. For these comparisons, we reference Oudmaijer et al. (2011) and Cauley & Johns-Krull (2014) for HAeBes (corresponding to intermediate-mass stars in Phase I) and Edwards et al. (2006) mainly for low-mass T Tauri stars. As for intermediate-mass stars, Oudmaijer et al. (2011) detected He I features in 79 out of 90 of their sample HAeBes. Although not all of their spectra are shown in their paper, the partially shown observed spectra (not residual profiles) show group PC, IPC, or DP profiles. Cauley & Johns-Krull (2014) observed 56 HAeBes, 28 HAe stars and 28 HBe stars. For HAe stars, whose mass range is roughly comparable to that of our targets in this paper, they detected He I features in 26 stars. We summarize the statistics of the profile morphology for their targets in Table 9 based on their Figure 4. As a result, the occurrence frequencies of groups PC and IPC are relatively higher than those of the other types. The statistics of HAe stars are not inconsistent with those of Phase I and Phase II sources in the intermediate-mass star sample in this study. Cauley & Johns-Krull (2014) pointed out that narrow blueshifted absorption features are not seen in HAe stars in their sample, while broad blueshifted absorption features are common. This tendency is also seen in our Phase I sources. Considering that narrow blueshifted absorption features are seen only in some Phase II objects in the sample of intermediate-mass stars (RY Tau, SU Aur, V773 Tau, and DS Tau), these features may be characteristics for Phase II objects.

As for low-mass stars, Edwards et al. (2006) detected He I features in 38 of 39 CTTSs in their sample. We show the statistics of He I profile morphology for low-mass stars from Edwards et al. (2006) in Table 9. CTTSs are categorized into almost all profile types. The occurrence frequency of group PC is highest, while that of group BR is second highest. Group PC

sources are observed in both Phase I and II sources in the intermediate-mass star sample, but group BR sources are only observed in Phase II sources. However, the statistics of CTTSs do not appear to differ significantly from those of Phase I and II sources in the intermediate-mass star sample. Edwards et al. (2006) suggested that broad P Cygni-like profiles are more common among stars of high veilings ($\gamma_{\gamma} \geq 0.5$), while narrow emission coupled with both blueshifted and redshifted absorption is more common among stars with low veilings ($\gamma_{\gamma} \leq 0.2$). This tendency agrees with the results of the intermediate-mass samples for He I profiles: group PC sources are more common in Phase I, while some sources with narrow emission and redshifted and blueshifted absorption features are seen only in Phase II. In contrast, we also show the statistics of He I profile morphology for WTTSs by Edwards et al. (2006), which are comparable to low-mass stars in Phase III, in Table 9. The highest occurrence frequency belongs to group F (featureless) for four sources, and the second highest is group E (pure emission) for two sources. This result is not consistent with those for our target intermediate-mass stars in Phase III, which is discussed later (Section 4.2.3).

4.2. Interpretation of $P\beta$ and He I Line Profile Morphologies

Paschen lines exhibit a centered emission peak and a redshifted absorption that can be used as diagnostics for magnetospheric accretion, while He I profiles show both blueshifted and redshifted absorptions that can be used as diagnostics for magnetospheric accretion flows and inner winds, respectively (Hartmann et al. 2016). We largely based our interpretations on the profile morphology of the $P\beta$ and He I line profile rather than on line width or intensity.

4.2.1. Magnetospheric Accretion

Both $P\beta$ and He I line profiles show redshifted absorptions that can be used as diagnostics for magnetospheric accretion (e.g., Folha & Emerson 2001; Edwards et al. 2006; Fischer et al. 2008; Kurosawa et al. 2011). First, we diagnose in which

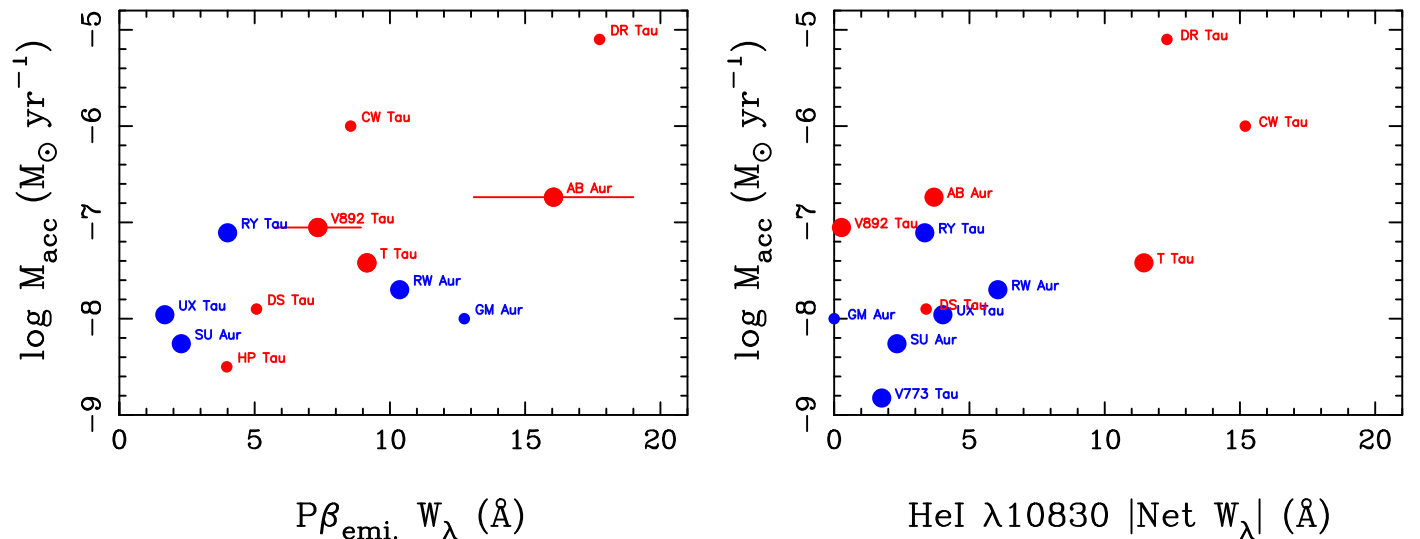


Figure 4. Equivalent width vs. mass accretion rate. The target intermediate-mass stars in this study are presented by large filled circles. Phase I and II sources are shown with red and blue, respectively. Six additional intermediate-mass stars in the samples of Folha & Emerson (2001) and Edwards et al. (2006) are denoted by small symbols with the same colors as that of the targets observed in the present study. The mass accretion rates for the targets observed in the present study are shown in Table 2, the rate for HP Tau is reported by Johns-Krull & Gafford (2002), and the rates for the five remaining additional sources are reported by Edwards et al. (2006). Left: $P\beta$ emission EW and mass accretion rate. Equivalent widths for the targets observed in the present study are shown in Table 6. The error bars of Phase I sources are for V892 Tau and AB Aur, showing the EWs in the case of $\gamma = 0.0$ and 2.0 (Section 3.3). The EWs for the additional sources are from Folha & Emerson (2001); those for HP Tau, GM Aur, and DS Tau (showing PC profiles) are obtained from Table 6 in that article, and those for CW Tau and DR Tau are roughly estimated from Figure 1 in that article. Right: Sum of absolute values of emission plus absorption He I EWs vs. mass accretion rate. The EWs for the targets observed in the present study are shown in Table 7 and those for the additional sources are from Table 1 of the study by Edwards et al. (2006).

sources magnetospheric accretions are functioning using the $P\beta$ line profiles. The line profiles for RW Aur, HP Tau, GM Aur, and DS Tau show redshifted subcontinuum features, displaying a clear magnetospheric accretion signature. For nine sources (V892 Tau, AB Aur, IRAS 04101+3103, T Tau, RY Tau, SU Aur, UX Tau, CW Tau, and DR Tau), the observed line profiles show emission features but do not show redshifted subcontinuum features. Four of these sources (V892 Tau, AB Aur, IRAS 04101+3103, and T Tau) are categorized into group E (pure emission), whereas five sources (RY Tau, SU Aur, UX Tau, CW Tau, and DR Tau) are categorized into group DP (double-peaked emission). Considering the sources in group E have $|V_{\max}^{\text{blue}}| > |V_{\max}^{\text{red}}|$ and that the sources in group DP, except for CW Tau, have $V_{\text{peak}}^{\text{em}} < 0$, they show slight influence from redward absorption features, suggesting that magnetospheric accretion activities are functioning. The model $\text{Br}\gamma$ line profiles¹⁴ for sources with magnetospheric accretion calculated by Muzerolle et al. (1998a) also show a redward absorption feature (not subcontinuum features) at inclination angles of $\lesssim 60^\circ$ (see their Figure 5). Therefore, the $P\beta$ observed line profiles suggest that magnetospheric accretion processes are functioning in the eight sources that exhibit emission features but not redshifted subcontinuum features, except for CW Tau, in addition to four sources that do exhibit redshifted subcontinuum features.

He I can also be used as diagnostics for magnetospheric accretion. The observed line profiles for five sources (V892 Tau, SU Aur, RW Aur, UX Tau, and DS Tau) show redshifted subcontinuum features, displaying a clear magnetospheric accretion signature. For the other sources in Phase I and II, except for GM Aur, the line profiles show He I emissions but do not show the redshifted subcontinuum features. This seems

to suggest that the activities of magnetospheric accretion are not functioning. However, Kurosawa et al. (2011) indicated that wind-related He I emissions are relatively minor, whereas the magnetosphere is a main emission contributor (see Figure 12 in Kurosawa et al. 2011). The line profiles for three sources (RY Tau, CW Tau, and HN Tau), which are categorized into group DP, also show redward absorption features, judging from $V_{\text{peak}}^{\text{em}} < 0$, suggesting magnetospheric accretion activities. Therefore, He I profiles for all Phase I and II sources, except for GM Aur, suggest magnetospheric activities.

In summary, all Phase I and II sources suggest magnetospheric activities from the observed line profiles of $P\beta$ and He I, although the profiles for approximately half of them (V892 Tau, SU Aur, RW Aur, UX Tau, HP Tau, GM Aur, and DS Tau) show redshifted subcontinuum features in $P\beta$ and/or He I lines, which are clear magnetospheric accretion signatures.

4.2.2. Inner Winds

He I profiles show both blueshifted and redshifted absorptions that can be used as diagnostics for magnetospheric accretion flows and inner winds, respectively (Hartmann et al. 2016). Kwan et al. (2007) modeled blueshifted absorption at He I $\lambda 10830$ in CTTS via scattering of the stellar and veiling continua as a probe of inner winds, while Kurosawa et al. (2011) presented multidimensional non-local thermodynamic equilibrium radiative transfer models of hydrogen and helium line profiles formed in the magnetospheric accretion and inner winds of CTTSs, including He I $\lambda 10830$ and $P\beta$. Both models are consistent with the scenario in which the narrow blueshifted absorption component of He I $\lambda 10830$ seen in observations is caused by a disk wind, and the wider blueshifted absorption component (the terminal velocity of the wind up to 400 km s^{-1}) is caused by stellar wind.

In the sample of intermediate-mass stars, the line profiles for seven sources (AB Aur, RY Tau, SU Aur, T Tau, V773 Tau, DR

¹⁴ $\text{Br}\gamma$ line profiles are known to show very similar features to $P\beta$ line profiles (Folha & Emerson 2001).

Tau, and DS Tau) have blueshifted subcontinuum absorption features. Of these, the line profiles for AB Aur, T Tau, and DR Tau are categorized into group PC with broad blueshifted subcontinuum absorption ($v_{\text{max}}^{\text{blue}} \sim -300$ to -400 km s $^{-1}$). They are consistent with the stellar wind case. The line profiles for RY Tau, SU Aur, V773 Tau, and DS Tau show narrow blueshifted subcontinuum absorption features, with terminal wind velocities of $\lesssim 150$ km s $^{-1}$. They are consistent with the disk wind case. The stellar wind is suggested to be functioning in AB Aur, T Tau, and DR Tau, whereas the disk wind is suggested to be functioning in RY Tau, SU Aur, V773 Tau, and DS Tau.

4.2.3. Phase III Sources

The observed $P\beta$ profiles show group F features (featureless), while the observed He I profiles for all Phase III sources show group A features (pure absorption) with centered subcontinuum absorption. These features are not expected in model profiles in the case of disk wind or stellar wind (e.g., Kurosawa et al. 2011). This suggests that these sources have no such activities. Moreover, because absorption features in He I are broader for sources with larger v_{broad} , the lines are more likely to be stellar intrinsic features than circumstellar features.

4.3. Progression of Dominant Processes with Evolution of Protoplanetary Disks

In Section 4.2, observed $P\beta$ and He I profiles for each source were interpreted. In Phase I, three sources (AB Aur, T Tau, and DR Tau) show features of stellar wind, while the other four sources (V892 Tau, IRAS 04101+3103, CW Tau, and HN Tau) show no features of inner winds. For magnetospheric accretion, only V892 Tau and HP Tau show clear features, while the other sources show features suggesting the activity. In Phase II, four sources (RY Tau, SU Aur, V773 Tau, and DS Tau) show features of disk wind, while the other three sources (RW Aur, UX Tau, and GM Aur) show no features of inner winds. For magnetospheric accretion, five sources (SU Aur, RW Aur, UX Tau, GM Aur, and DS Tau) show clear features, while the other two sources show the feature suggesting the activities. In Phase III, no targets show activities of mass accretion, disk winds, or stellar winds. This suggests that the dominant processes in different evolutionary phases are different, particularly for inner winds. This finding indicates a progression of dominant mass-flow processes with disk evolution: stellar wind and probably magnetospheric accretion in Phase I, magnetospheric accretion and disk wind in Phase II, and no activities in Phase III. In particular, progression is observed for inner winds. The statistics of the blueshifted absorption types for He I lines, broad or narrow, which are used for diagnostics of dominant inner winds, are summarized in Table 9.

However, some points still need to be considered. (i) YSOs tend to be variable, which can cause line profiles to differ in the observation periods (Bouvier et al. 2003). Previous studies suggest that the general features of the observed line profiles do not change between periods, although the lines can show $\sim 10\%$ variabilities (e.g., Kurosawa et al. 2005; Edwards et al. 2006). However, the times between observations were not very long (a year at longest in the study conducted by Edwards et al. 2006). In contrast, the $P\beta$ line profile morphologies reported by Folha & Emerson (2001) and the $P\gamma$ line profile morphologies reported by Edwards et al. (2006) for the same sources show

clear difference (e.g., those of CW Tau and DR Tau; see Table 3). Considering that the $P\gamma$ morphology of the profile is known to be reminiscent of the $P\beta$ profile (Edwards et al. 2006, see also Section 3.1), the line profiles can vary by approximately seven years, reported for the Paschen series, which has a long time separation (1994–1995 by Folha & Emerson 2001 and 2001–2002 by Edwards et al. 2006). Therefore, continuous observation of He I is necessary in the future. (ii) The targets in this study are limited to only 19 sources. Eleven sources are excluded due to limited instrumental sensitivities, but they satisfy the other conditions for selecting the target intermediate-mass stars (Section 2.1). A large fraction of the excluded sources are of the latest spectral type, K5, according to the criteria for selecting the intermediate-mass stars. Because each spectral type corresponds to a certain range of star masses and ages, the sources should have marginal masses between low mass and intermediate mass (Yasui et al. 2014). Thus, the exclusion may not be necessarily bad to avoid contaminating the sample of low-mass stars. However, because the excluded sources may alter the statistics, more observations are necessary in the future. To investigate the universality of the suggested progression, YSOs of a wide variety of ages and masses should be observed. (iii) The spectral types of Phase I targets appear earlier (three A- or B-type and five K-type stars) than those of Phase II and III targets (G- to K-type stars). This bias may impact observed profiles, influencing our interpretation of dominant activities in each source and phase. However, such tendencies are not necessarily true for all intermediate-mass sources observed in this study, e.g., the later spectral type of T Tau (K0) than those of HP Tau/G2 (G0), RY Tau (G1), SU Aur (G1), and HD 283572 (G5). Also, such tendencies are not seen in the six intermediate-mass stars in the samples of Folha & Emerson (2001) and Edwards et al. (2006) (see Section 2.1). Therefore, the differences in spectral type should not generate a systematic bias. (iv) From Tables 2 and 5, Phase I sources appear to have higher mass accretion rates. We plot $P\beta$ and He I EWs versus mass accretion rate for our intermediate-mass targets with measured mass accretion rate in Figure 4. Sources of Phase I and II are indicated in red and blue, respectively. $P\beta$ emission EWs are shown in the left panel. The figure suggests that $P\beta$ emission EWs are moderately correlated with mass accretion rate ($p = 0.66$), as suggested in Folha & Emerson (2001), and that Phase I sources seem to have larger mass accretion. This may suggest that the mass accretion rate determines the dominant activities of inner winds. However, such tendencies are not necessarily true for all sources, e.g., T Tau (Phase I) has a smaller mass accretion rate than that of RY Tau (Phase II) for the targets observed in the present study, and the mass accretion rates of HP Tau and DS Tau (Phase I) are smaller than or comparable to those for Phase II sources. This is also discussed in Section 4.4 in the context of previous studies (e.g., Edwards et al. 2006). For reference, we also plot the sum of absolute values of emission and absorption of He I EWs, which is introduced by Edwards et al. (2006), versus mass accretion rate (Figure 4, right panel). This shows that the equivalent values of He I are also correlated with mass accretion rate ($p = 0.75$), which Edwards et al. (2006) specified using their sample CTTSs. (v) Finally, the weakening of stellar wind signatures and strengthening of disk wind signatures in Phase II may be due solely to an overall weakening in stellar wind activities through the disk evolution. Kwan et al. (2007)

indicated that excitation conditions for He I $\lambda 10830$ are more favorable in stellar wind than in disk wind. In any case, the suggested progression does not change significantly: stellar winds (and possibly disk winds as well) are active at first, and then disk winds become relatively active. However, further quantitative approaches using the fitting of observed profiles with model profiles are necessary in future work.

4.4. Comparison of Suggested Progression of Dominant Processes with Previous Studies

Although we were unable to find previous results for high-resolution spectroscopy of young intermediate-mass stars with both He I and P β , the He I profiles for HAeBes are presented in Cauley & Johns-Krull (2014). For H Ae stars, whose mass range is roughly comparable to that of our targets, the statistics of their P β and He I line profile morphologies are not significantly different from those of Phase I and II sources, as discussed in Section 4.1. Cauley & Johns-Krull (2014) pointed out that in H Ae stars, disk winds (evidenced by narrow blueshifted absorption features) are not functioning, while stellar winds (evidenced by commonly broad blueshifted absorption features) are functioning. A summary of the statistics of the He I blueshifted subcontinuum absorption features for the H Ae stars is presented in Table 9. These results are consistent with our results for Phase I sources. Admittedly, our data set has a small sample size (seven Phase I sources). The agreement between the results of their large sample (28 H Ae stars) and those of our smaller sample reinforces the suggestion, however, that dominant processes for Phase I are stellar wind and probably magnetospheric accretion.

Previous authors have posited alternative mechanisms for the progression of dominant processes. Edwards et al. (2006) mainly focused on veilings as an indicator of disk evolutionary phases because veilings are suggested to be correlated with mass accretion rate. Kwan et al. (2007) used a comparison of their theoretical line profiles with observed profiles from Edwards et al. (2006). They identified 11 and 15 CTTSs with blueshifted absorption features that resemble the disk wind models and stellar wind models, respectively. A summary of the statistics of the He I absorption features for CTTSs is presented in Table 9. Edwards et al. (2006) suggested that stars with high disk accretion rates are more likely to have stellar wind signatures than disk wind signatures. However, note that CTTSs in all veiling groups show morphological features of group PC, with broad redshifted absorption suggesting stellar wind, even with the lowest observed veiling, $\gamma_V \leq 0.2$. In addition, all groups show profiles with narrow absorption features suggesting disk wind, even with the highest observed veiling, $\gamma_V \geq 0.5$ (see Figure 10 in Edwards et al. 2006). This set of observations suggests that the trend is not so significant. We find this unsurprising because the veiling, and thus the mass accretion rate, will not necessarily be a clear indicator of disk evolution, as discussed in Section 2.1. As a result, a clear progression of profile morphologies with veilings is not observed.

4.5. Chromospheric Activities in Phase III Sources

In Section 4.2.3, Phase III sources were suggested to show no activities for mass accretion or inner winds. This is consistent with WTTs reported in Edwards et al. (2006). WTTs are known to exhibit high levels of chromospheric and coronal features (Stelzer et al. 2013), which persist at the age of

$\sim 50\text{--}100$ Myr (Stauffer et al. 1994). The chromospheric profile has often been observed as emission lines in X-ray and optical lines such as the H α , H β , Ca II, and Na I lines. Chromospheric activities are also recognized from He I $\lambda 10830$ absorption lines (e.g., Vaughan & Zirin 1968), and are suggested to persist for star ages as advanced as those of Population II stars (Takeda & Takada-Hidai 2011). We suggest that the He I absorption features detected here are most likely to be chromospheric features, considering that Phase III sources are almost comparable to WTTs (Yasui et al. 2014) and that the observed He I features in this paper are suggested to be stellar intrinsic features (see Section 4.2.3). Note that the centered subcontinuum absorption features are not necessarily indicative of the chromospheric activities. When the features are accompanied by emissions the profiles are categorized into group DP (e.g., IRAS 04101+3103). Cauley & Johns-Krull (2014) suggested that the profiles are most likely to be formed because of Keplerian rotation very close to the stellar surface. Also, it should be noted that the photospheric features have little impact on the He I residual profiles. Figure 5 shows synthetic spectra, observed spectra, and residual profiles for all four Phase III sources. Three photospheric features are observed in the spectral region, Mg I $\lambda 10814.1$ and Si I ($\lambda 10830.1$ and $\lambda 10846.8$); of these, only Si I $\lambda 10830.1$ profiles appear to cover the He I profile. However, the line is very shallow for HP Tau/G2, HD 283572, and V410 Tau because of the large v_{broad} , ~ 100 km s $^{-1}$, while the line barely covers the He I profile for HBC 388 because of the small v_{broad} , 25 km s $^{-1}$. Figure 5 suggests that the photospheric features are moderately removed by subtracting synthetic spectra from observed spectra (Section 3.2).

The He I line is a transition between lower metastable level of 2^3S and the upper level of 2^3P . Two mechanisms have been proposed for populating the upper levels of He I: photoionization-recombination (PR) mechanism via EUV and X-ray radiations (Goldberg 1939), and electron collisions from the ground level (Andretta & Jones 1997). The existence or absence of correlation between He I absorption and X-ray luminosity can discern which process is dominant (Zarro & Zirin 1986); the correlation exists when the PR mechanism is dominant, while the correlation is absent when collisional excitation is dominant. We show fractional X-ray luminosities (L_X/L_{bol}) versus He I absorption EWs for all Phase III sources in Figure 6. Equivalent widths are obtained from Table 7, whereas L_X/L_{bol} is obtained from previous studies (Güdel et al. 2007; Wichmann et al. 1996). All Phase III sources have L_X/L_{bol} in the very small range of -3.4 to -3.5 , whereas EWs span $\sim 0.5\text{--}1.5$. For comparison, we also show the results from Zarro & Zirin (1986) in Figure 6. These authors presented the correlation in dwarfs and giants. Thus, EW and L_X/L_{bol} are not correlated in Phase III sources, suggesting that the dominant mechanism for these sources is electron collisions rather than the PR mechanism. Phase I and II sources are plotted in Figure 6 for reference, although we were unable to find any literature references for the value of IRAS 04101+3103.

The He I absorption features associated with chromospheric activities have to our knowledge not previously been reported for YSOs. In Edwards et al. (2006), no WTTs show He I absorption features although He I line profiles for two WTTs show emission features (see Section 3.4), and these authors surmised that these features arise in an active chromosphere or in very weak accretion. We suggest that the features detected even in such young phases

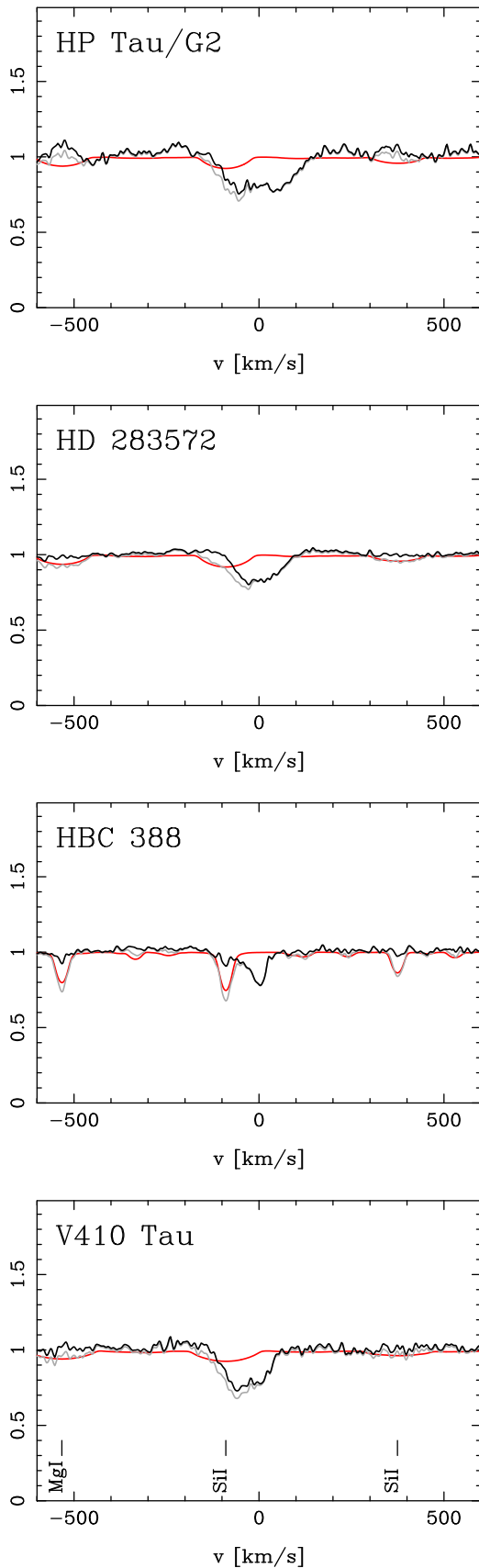


Figure 5. He I $\lambda 10830$ spectra for Phase III sources. The synthetic spectra, observed spectra, and residual profiles are shown with red, gray, and black lines, respectively. Photospheric features, Mg I $\lambda 10814.1$ and Si I ($\lambda 10830.1$ and $\lambda 10846.8$), are marked with vertical lines in the panel of V410 Tau (bottom).

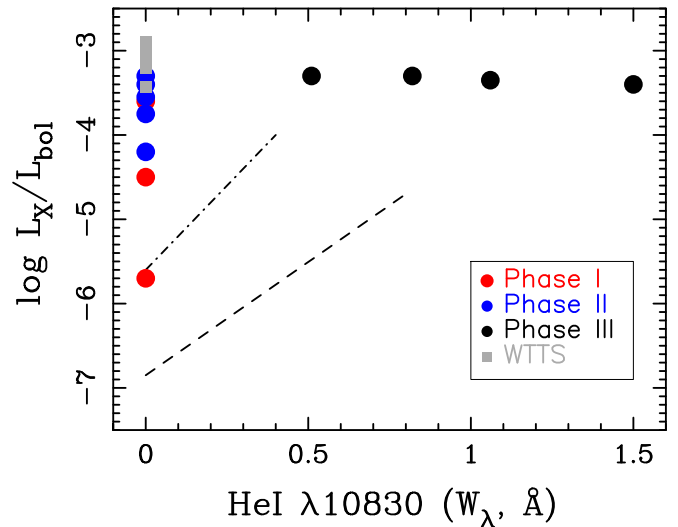


Figure 6. The fractional X-ray luminosities (L_X/L_{bol}) vs. He I absorption EWs. Phase I, II, and III sources are shown by red, blue, and black circles, respectively, while the WTTs in the sample of Edwards et al. (2006) are shown by gray squares. The lines show linear fits to sample stars in Zarro & Zirin (1986) by Sanz-Forcada & Dupree (2008); the dot-dashed line is for dwarfs and subgiants, and the dashed line is for all giants.

are characteristics of intermediate-mass stars, considering that these authors' targets were primarily low-mass stars and that all of our intermediate-mass star targets in Phase III show the He I absorption features. This pattern may be due solely to a positive correlation between stellar mass and X-ray luminosities (Güdel et al. 2007), which can be correlated with chromospheric activities. We show L_X/L_{bol} values of the WTTs in Edwards et al. (2006) in Figure 6 (gray squares). The L_X/L_{bol} values for the WTTs (-3.4 to -2.9 ; Güdel et al. 2007; Bertout et al. 2007; Yang et al. 2012; Kastner et al. 2016, 2004) are comparable to those of our Phase III sources. Therefore, the reason for the detection of He I chromospheric absorption features only in our intermediate-mass targets in Phase III is not likely the correlation between stellar mass and X-ray luminosities.

Correlations of chromospheric and higher-temperature features with stellar age, magnetic field, and rotation period properties have previously been reported (Linsky 2017). For the first factor, the He I absorption features are not seen in the sample WTTs of Edwards et al. (2006), which are also the sources in the same star-forming-region as our targets, i.e., the Taurus star-forming region. Therefore, stellar age does not seem to be the cause for the He I detection in Phase III sources. For the second factor, although there are only a limited number of derivations of magnetic fields, there seem to be no significant differences between those for our Phase III sources and the WTTs reported in Edwards et al. (2006): ~ 0.5 – 1.5 kG for HBC 388 and V410 Tau (Basri et al. 1992; Skelly et al. 2010), ~ 0.5 – 2 kG for LkCa 4, V891 Tau, and V827 Tau (Donati et al. 2014, 2015; Giardino et al. 2006). Therefore, the magnetic field may not likely to be the cause for the He I detection in Phase III sources. For the last factor, i.e., rotation, Phase III sources generally have large $v \sin i$, ~ 100 km s $^{-1}$ (Table 5), while the WTTs in the sample of Edwards et al. (2006) generally have small $v \sin i$ values, < 20 km s $^{-1}$ (Rebull et al. 2004). Most theoretical models of stellar magnetic dynamos predict increasing magnetic flux emerging through stellar photospheres with larger rotation velocities (Linsky 2017). This

suggests that the larger rotation velocities may be the possible cause for the detection of He I absorptions in Phase III sources.

4.6. Implication to Theories of Mass-flow Processes

Although configurations of mass-flow processes around central stars have been proposed, we do not yet have a conclusive theory explaining angular momentum transport in the star formation process. From the suggested progression of dominant mass-flow processes with the evolution of protoplanetary disks in Section 4.3, we discuss what factors determine which processes dominate, or in which physical conditions one dominates the other. These connections may help place useful constraints on current theories.

Before we discuss this, it is necessary to pay attention to whether intermediate-mass stars can be regarded as simply massive T Tauri stars. Cauley & Johns-Krull (2014) presented high-resolution He I observations of HAeBes, which correspond to intermediate-mass stars in Phase I. They suggested that HAe stars, whose mass range is roughly comparable to that of our targets, cannot be regarded as massive CTTSs because they do not show signatures of magnetospheric accretion and inner winds in the same manner as CTTSs: HAe stars show signatures of magnetospheric accretion and stellar winds, but do not show signatures of disk winds.¹⁵ The authors pointed out the possibility that the magnetospheres might be smaller, based on the paucity of detected magnetic fields for HAeBes, compared to CTTSs. They confirmed small magnetospheres from their results that maximum absorption velocities in the redshifted absorption profiles in their sample are a smaller fraction of the system escape velocity than in CTTSs. They suggested that the small magnetospheres may be less efficient at driving disk winds than CTTS magnetospheres. The similar trends are also suggested for CTTSs by Kwan et al. (2007): stars with the highest disk accretion rates are less likely to have redshifted absorption from magnetospheric funnel flows. They suggested that their disks have small magnetospheres, which may set up favorable conditions for stellar wind rather than disk wind. The maximum redshifted absorption velocities in all obtained He I line profiles of both Phase I and II sources in our intermediate-mass targets having redshifted absorption features are estimated to be as small as those of HAe stars, $<400 \text{ km s}^{-1}$. Assuming stellar radii of our targets (stellar mass of $\gtrsim 1.5 M_{\odot}$) based on the isochrone model at the age of 1.5 Myr by Siess et al. (2000), escape velocities of our targets are calculated to be $\gtrsim 500 \text{ km s}^{-1}$. The fraction of the system escape velocity estimated with the above velocities (i.e., the maximum redshifted absorption velocities and escape velocities) for our targets is smaller than for CTTSs, corresponding to ballistic infall from distances of $<2 R_{\odot}$ toward central stars. This is again consistent with that for HAe stars (see Figure 5 in Cauley & Johns-Krull 2014). This suggests that magnetospheres of intermediate-mass stars are generally smaller than those of CTTSs. Nonetheless, signatures of disk winds are seen in Phase II sources, although the same trends (signatures of stellar winds) as seen in HAe stars are seen in Phase I sources. This suggests that the lack of disk wind signatures in HAe stars is not a characteristic of intermediate-mass stars, but only of HAe stars, or Phase I sources. Furthermore, there should be

another factor that functions more effectively than magnetosphere size for determining dominant mass-flow processes.

The inner part of a protoplanetary disk in Phase II has low opacity and is where most dust settling or growth is expected to occur. In contrast, the inner disk in Phase I has high opacity but without substantial dust settling or growth (Yasui et al. 2014). Owing to the low opacity in Phase II, radiation from central stars can penetrate deeply into disks, and thus the ionization fraction should be higher. This may be the reason why disk winds are active in Phase II. This interpretation is consistent with the theory of the disk wind in which a sufficient magnetic field and ionization fraction launch magnetocentrifugal winds over a significant range of radii in the disk, from an inner truncation radius out to several astronomical units (Oued & Pudritz 1997). In addition, Phase III stars, having already lost their entire dust disks, show profiles with no signature of accretion or of inner winds. The absence of these signatures in Phase III, along with the presence of these signatures in Phase I and II, is consistent with the previous suggestion that inner winds (stellar winds and disk winds) are accretion driven.

5. Conclusion

We performed NIR high-resolution ($R = 28,000$) spectroscopy of 13 young intermediate-mass stars in the Taurus star-forming region with WINERED. Our obtained spectra ($\lambda = 0.91\text{--}1.35 \mu\text{m}$) depict He I $\lambda 10830$ and $P\beta$ lines, which are sensitive to magnetospheric accretion and winds. We investigate five sources each for $P\beta$ and He I lines from previous studies, in addition to the 13 targets observed in this study. Based on the presence of NIR and MIR continuum emission, young intermediate-mass stars can be classified into three different evolutionary stages: Phases I, II, and III, in the order of evolution.

1. Phase I and II sources exhibit a variety of profile morphologies in $P\beta$, while all Phase III sources are in group F (i.e., they are featureless). The statistics of the $P\beta$ profile morphologies for Phase I and Phase II sources are not significantly different, except that almost half of the Phase I sources show group E features, while none of the Phase II sources exhibit the features. The statistics of Phase I and II sources are consistent with those of low-mass CTTSs. Furthermore, the morphology statistics for Phase III sources are not inconsistent with those of low-mass WTTSs.
2. Phase I and II sources also show a variety of He I profile morphologies. The profile morphologies of Phase I and Phase II sources are mostly broad subcontinuum absorption lines and narrow subcontinuum absorption lines, respectively; however, the statistics of these profile morphologies are not significantly different and are comparable to those of low-mass CTTSs. In contrast, all Phase III sources are in group A (i.e., they exhibit pure absorption) with centered subcontinuum absorption features. This is inconsistent with the characteristics of low-mass WTTSs.
3. By comparing observed $P\beta$ and He I line profiles with model profiles, we suggest that dominant mass-flow processes are stellar wind and probably magnetospheric accretion in Phase I, magnetospheric accretion and disk wind in Phase II, and no activities in Phase III.

¹⁵ Cauley & Johns-Krull (2014) suggested that HBe stars do not show signatures of magnetospheric accretion and disk winds in general, but show signatures of stellar winds.

4. The different dominant processes in different phases indicate a clear progression of dominant mass-flow processes with disk evolution. However, because this study may not contain a statistically significant number of sources, more statistical studies are necessary to draw a firm conclusion.
5. The mass-flow processes in HAe stars are consistent with Phase I, with stellar wind as the dominant process. As for the progression of mass-flow processes, the trends in veilings found by other authors do not seem so significant compared to the trend suggested in this paper based on disk evolutionary phase. Although the absence of activities in Phase III is consistent with previous studies for low-mass WTTSs, we note that He I line profiles do show chromospheric activities in these sources.
6. Disk wind signatures are seen in Phase II sources, despite their smaller magnetospheres, which was suggested to be the reason for the absence of the signature in HAe stars by other authors. Alternatively, we suggest that opacity in protoplanetary disks plays an important role in determining dominant mass-flow processes.

We thank an anonymous referee for helpful comments that improved the manuscript. We are grateful to the staff of Koyama Astronomical Observatory for their support during our observation. C.Y. is supported by KAKENHI (18H05441) Grant-in-Aid for Scientific Research on Innovative Areas. S.H. is supported by Grant-in-Aid for JSPS Fellows Grant No. 13J10504. K.F. is supported by KAKENHI (16H07323) Grant-in-Aid for Research Activity start-up. N.K. is supported by JSPS-DST under the Japan-India Science Cooperative Programs during 2013–2015 and 2016–2018. This study is financially supported by JSPS KAKENHI (16684001) Grant-in-Aid for Young Scientists (A), JSPS KAKENHI (20340042) Grant-in-Aid for Scientific Research (B), JSPS KAKENHI (21840052) Grant-in-Aid for Young Scientists (Start-up), and MEXT Supported Program for the Strategic Research Foundation at Private Universities, 2008–2012 (No. S0801061) and 2014–2018 (No. S1411028). This work has made use of the VALD database, operated at Uppsala University, the Institute of Astronomy RAS in Moscow, and the University of Vienna.

ORCID iDs

Satoshi Hamano  <https://orcid.org/0000-0002-6505-3395>
 Hiroaki Sameshima  <https://orcid.org/0000-0001-6401-723X>
 Yuji Ikeda  <https://orcid.org/0000-0003-2380-8582>
 Hideyo Kawakita  <https://orcid.org/0000-0003-2011-9159>
 Daisuke Taniguchi  <https://orcid.org/0000-0002-2861-4069>
 Misaki Mizumoto  <https://orcid.org/0000-0003-2161-0361>
 Natsuko Izumi  <https://orcid.org/0000-0003-1604-9127>

References

- Akeson, R. L., Ciardi, D. R., van Belle, G. T., & Creech-Eakman, M. J. 2002, *ApJ*, 566, 1124
- Alecian, E., Wade, G. A., Catala, C., et al. 2013, *MNRAS*, 429, 1001
- Andretta, V., & Jones, H. P. 1997, *ApJ*, 489, 375
- Andrews, S. M., & Williams, J. P. 2005, *ApJ*, 631, 1134
- Andrews, S. M., Wilner, D. J., Espaillat, C., et al. 2011, *ApJ*, 732, 42
- Ansdell, M., Williams, J. P., Manara, C. F., et al. 2017, *AJ*, 153, 240
- Ardila, D. R., Basri, G., Walter, F. M., Valenti, J. A., & Johns-Krull, C. M. 2002, *ApJ*, 566, 1100
- Barrado y Navascués, D., & Martín, E. L. 2003, *AJ*, 126, 2997
- Basri, G., Marcy, G. W., & Valenti, J. A. 1992, *ApJ*, 390, 622
- Beristain, G., Edwards, S., & Kwan, J. 2001, *ApJ*, 551, 1037
- Bertout, C., & Genova, F. 2006, *A&A*, 460, 499
- Bertout, C., Siess, L., & Cabrit, S. 2007, *A&A*, 473, L21
- Bessell, M. S., & Brett, J. M. 1988, *PASP*, 100, 1134
- Bodenheimer, P. 1995, *ARA&A*, 33, 199
- Bouvier, J., Covino, E., Kovo, O., et al. 1995, *A&A*, 299, 89
- Bouvier, J., Grankin, K. N., Alencar, S. H. P., et al. 2003, *A&A*, 409, 169
- Calvet, N., & Hartmann, L. 1992, *ApJ*, 386, 239
- Calvet, N., Muzerolle, J., Briceño, C., et al. 2004, *AJ*, 128, 1294
- Cauley, P. W., & Johns-Krull, C. M. 2014, *ApJ*, 797, 112
- Corder, S., Eisner, J., & Sargent, A. 2005, *ApJL*, 622, L133
- Donati, J.-F., Hébrard, E., Hussain, G., et al. 2014, *MNRAS*, 444, 3220
- Donati, J.-F., Hébrard, E., Hussain, G. A. J., et al. 2015, *MNRAS*, 453, 3706
- Donati, J. F., Moutou, C., Malo, L., et al. 2016, *Natur*, 534, 662
- Donehew, B., & Brittain, S. 2011, *AJ*, 141, 46
- Dong, R., Najita, J. R., & Brittain, S. 2018, *ApJ*, 862, 103
- Edwards, S., Fischer, W., Hillenbrand, L., & Kwan, J. 2006, *ApJ*, 646, 319
- Espaillat, C., D'Alessio, P., Hernández, J., et al. 2010, *ApJ*, 717, 441
- Fischer, W., Kwan, J., Edwards, S., & Hillenbrand, L. 2008, *ApJ*, 687, 1117
- Folha, D. F. M., & Emerson, J. P. 1999, *A&A*, 352, 517
- Folha, D. F. M., & Emerson, J. P. 2001, *A&A*, 365, 90
- Furlan, E., Hartmann, L., Calvet, N., et al. 2006, *ApJS*, 165, 568
- Furlan, E., Luhman, K. L., Espaillat, C., et al. 2011, *ApJS*, 195, 3
- García López, R., Natta, A., Testi, L., & Habart, E. 2006, *A&A*, 459, 837
- Giardino, G., Favata, F., Silva, B., et al. 2006, *A&A*, 453, 241
- Goldberg, L. 1939, *ApJ*, 89, 673
- Grady, C. A., Woodgate, B., Bruhweiler, F. C., et al. 1999, *ApJL*, 523, L151
- Gray, D. F. 2005, *The Observation and Analysis of Stellar Photospheres* (3rd ed.; Cambridge: Cambridge Univ. Press)
- Gray, R. O., Graham, P. W., & Hoyt, S. R. 2001, *AJ*, 121, 2159
- Güdel, M., Briggs, K. R., Arzner, K., et al. 2007, *A&A*, 468, 353
- Hamidouche, M. 2010, *ApJ*, 722, 204
- Hartigan, P., Hartmann, L., Kenyon, S., Hewett, R., & Stauffer, J. 1989, *ApJS*, 70, 899
- Hartmann, L. 2008, *PhST*, 130, 014012
- Hartmann, L. 2009, in *Accretion Processes in Star Formation*, ed. H. Lee (2nd ed.; Cambridge: Cambridge Univ. Press), 2009
- Hartmann, L., Avrett, E., & Edwards, S. 1982, *ApJ*, 261, 279
- Hartmann, L., Calvet, N., Gullbring, E., & D'Alessio, P. 1998, *ApJ*, 495, 385
- Hartmann, L., Herczeg, G., & Calvet, N. 2016, *ARA&A*, 54, 135
- Hartmann, L., Megeath, S. T., Allen, L., et al. 2005, *ApJ*, 629, 881
- Hatzes, A. P. 1995, *ApJ*, 451, 784
- Herbst, T. M., Robberto, M., & Beckwith, S. V. W. 1997, *AJ*, 114, 744
- Herbst, W. 1989, *AJ*, 98, 2268
- Hernández, J., Hartmann, L., Calvet, N., et al. 2008, *ApJ*, 686, 1195
- Ikeda, Y., Kobayashi, N., Kondo, S., et al. 2016, *Proc. SPIE*, 9908, 99085Z
- Ikeda, Y., Kobayashi, N., Kondo, S., et al. 2018, *Proc. SPIE*, 10702, 107025U
- Ingleby, L., Calvet, N., Herczeg, G., et al. 2013, *ApJ*, 767, 112
- Isella, A., Carpenter, J. M., & Sargent, A. I. 2010, *ApJ*, 714, 1746
- Johns-Krull, C. M., & Gafford, A. D. 2002, *ApJ*, 573, 685
- Joncour, I., Bertout, C., & Bouvier, J. 1994a, *A&A*, 291, L19
- Joncour, I., Bertout, C., & Menard, F. 1994b, *A&A*, 285, L25
- Kastner, J. H., Huenemoerder, D. P., Schulz, N. S., et al. 2004, *ApJL*, 605, L49
- Kastner, J. H., Principe, D. A., Punzi, K., et al. 2016, *AJ*, 152, 3
- Kennedy, G. M., & Kenyon, S. J. 2009, *ApJ*, 695, 1210
- Kenyon, S. J., Gómez, M., & Whitney, B. A. 2008, in *Handbook of Star Forming Regions, Volume I: The Northern Sky*, Vol. 4, ed. B. Reipurth (San Francisco, CA: ASP), 405
- Kenyon, S. J., & Hartmann, L. 1995, *ApJS*, 101, 117
- Kondo, S., Ikeda, Y., Kobayashi, N., et al. 2015, arXiv:1501.03403
- Kurosawa, R., Harries, T. J., & Symington, N. H. 2005, *MNRAS*, 358, 671
- Kurosawa, R., & Romanova, M. M. 2012, *MNRAS*, 426, 2901
- Kurosawa, R., Romanova, M. M., & Harries, T. J. 2011, *MNRAS*, 416, 2623
- Kurucz, R. 1993, *Diatomic Molecular Data for Opacity Calculations*, Kurucz CD-ROM No. 15 (Cambridge, MA: Smithsonian Astrophysical Observatory)
- Kwan, J., Edwards, S., & Fischer, W. 2007, *ApJ*, 657, 897
- Linsky, J. L. 2017, *ARA&A*, 55, 159
- Liu, T., Zhang, H., Wu, Y., Qin, S.-L., & Miller, M. 2011, *ApJ*, 734, 22
- Meléndez, J., & Barbuy, B. 1999, *ApJS*, 124, 527
- Monnier, J. D., Tannirkulam, A., Tuthill, P. G., et al. 2008, *ApJL*, 681, L97
- Mooley, K., Hillenbrand, L., Rebull, L., Padgett, D., & Knapp, G. 2013, *ApJ*, 771, 110
- Mundt, R. 1984, *ApJ*, 280, 749

- Muzerolle, J., Calvet, N., & Hartmann, L. 1998a, *ApJ*, 492, 743
Muzerolle, J., Calvet, N., & Hartmann, L. 2001, *ApJ*, 550, 944
Muzerolle, J., Calvet, N., Hartmann, L., & D'Alessio, P. 2003, *ApJL*, 597, L149
Muzerolle, J., D'Alessio, P., Calvet, N., & Hartmann, L. 2004, *ApJ*, 617, 406
Muzerolle, J., Hartmann, L., & Calvet, N. 1998b, *AJ*, 116, 2965
Oudmaijer, R. D., van den Ancker, M. E., Baines, D., et al. 2011, *AN*, 332, 238
Ouyed, R., & Pudritz, R. E. 1997, *ApJ*, 482, 712
Rebull, L. M., Wolff, S. C., & Strom, S. E. 2004, *AJ*, 127, 1029
Reipurth, B., Pedrosa, A., & Lago, M. T. V. T. 1996, *A&AS*, 120, 229
Rice, J. B., & Strassmeier, K. G. 1996, *A&A*, 316, 164
Rieke, G. H., & Lebofsky, M. J. 1985, *ApJ*, 288, 618
Ryabchikova, T., Piskunov, N., Kurucz, R., et al. 2015, *PhysS*, 90, 054005
Sameshima, H., Matsunaga, N., Kobayashi, N., et al. 2018, *PASP*, 130, 074502
Sanz-Forcada, J., & Dupree, A. K. 2008, *A&A*, 488, 715
Shu, F., Najita, J., Ostriker, E., et al. 1994, *ApJ*, 429, 781
Siess, L., Dufour, E., & Forestini, M. 2000, *A&A*, 358, 593
Simon, M. N., Pascucci, I., Edwards, S., et al. 2016, *ApJ*, 831, 169
Skelly, M. B., Donati, J.-F., Bouvier, J., et al. 2010, *MNRAS*, 403, 159
Skrutskie, M. F., Cutri, R. M., Stiening, R., et al. 2006, *AJ*, 131, 1163
Stauffer, J. R., Caillault, J.-P., Gagne, M., Prosser, C. F., & Hartmann, L. W. 1994, *ApJS*, 91, 625
Stelzer, B., Frasca, A., Alcalá, J. M., et al. 2013, *A&A*, 558, A141
Strassmeier, K. G. 1994, *A&A*, 281, 395
Strassmeier, K. G., Bartus, J., Kovari, Z., Weber, M., & Washuettl, A. 1998, *A&A*, 336, 587
Takagi, Y., Itoh, Y., Oasa, Y., & Sugitani, K. 2011, *PASJ*, 63, 677
Takeda, Y. 1995, *PASJ*, 47, 287
Takeda, Y., & Kawanomoto, S. 2005, *PASJ*, 57, 45
Takeda, Y., Sato, B., & Murata, D. 2008, *PASJ*, 60, 781
Takeda, Y., & Takada-Hidai, M. 2011, *PASJ*, 63, 547
Tang, Y.-W., Guilloteau, S., Piétu, V., et al. 2012, *A&A*, 547, A84
Ustyugova, G. V., Koldoba, A. V., Romanova, M. M., Chechetkin, V. M., & Lovelace, R. V. E. 1995, *ApJL*, 439, L39
Vaughan, A. H., Jr., & Zirin, H. 1968, *ApJ*, 152, 123
Weaver, W. B. 1987, *ApJL*, 319, L89
White, R. J., & Ghez, A. M. 2001, *ApJ*, 556, 265
Wichmann, R., Krautter, J., Schmitt, J. H. M. M., et al. 1996, *A&A*, 312, 439
Williams, J. P., & Cieza, L. A. 2011, *ARA&A*, 49, 67
Winn, J. N., & Fabrycky, D. C. 2015, *ARA&A*, 53, 409
Wittkowski, M., Schöller, M., Hubrig, S., Posselt, B., & von der Lühse, O. 2002, *AN*, 323, 241
Yang, H., Herczeg, G. J., Linsky, J. L., et al. 2012, *ApJ*, 744, 121
Yasui, C., Kobayashi, N., Tokunaga, A. T., & Saito, M. 2014, *MNRAS*, 442, 2543
Yasui, C., Kondo, S., Ikeda, Y., et al. 2008, *Proc. SPIE*, 7014, 701433
Yoshikawa, T., Ikeda, Y., Fujishiro, N., et al. 2012, *Proc. SPIE*, 8444, 84446G
Zarro, D. M., & Zirin, H. 1986, *ApJ*, 304, 365